LETTER

doi:10.1038/nature13697

Structure and evolution of the lunar Procellarum region as revealed by GRAIL gravity data

Jeffrey C. Andrews-Hanna[1], Jonathan Besserer[2], James W. Head III[3], Carly J. A. Howett[4], Walter S. Kiefer[5], Paul J. Lucey[6], Patrick J. McGovern[5], H. Jay Melosh[7], Gregory A. Neumann[8], Roger J. Phillips[4], Paul M. Schenk[5], David E. Smith[9], Sean C. Solomon[10,11] & Maria T. Zuber[9]

The Procellarum region is a broad area on the nearside of the Moon that is characterized by low elevations[1], thin crust[2], and high surface concentrations of the heat-producing elements uranium, thorium, and potassium[3,4]. The region has been interpreted as an ancient impact basin approximately 3,200 kilometres in diameter[5–7], although supporting evidence at the surface would have been largely obscured as a result of the great antiquity and poor preservation of any diagnostic features. Here we use data from the Gravity Recovery and Interior Laboratory (GRAIL) mission[8] to examine the subsurface structure of Procellarum. The Bouguer gravity anomalies and gravity gradients reveal a pattern of narrow linear anomalies that border Procellarum and are interpreted to be the frozen remnants of lava-filled rifts and the underlying feeder dykes that served as the magma plumbing system for much of the nearside mare volcanism. The discontinuous surface structures that were earlier interpreted as remnants of an impact basin rim are shown in GRAIL data to be a part of this continuous set of border structures in a quasi-rectangular pattern with angular intersections, contrary to the expected circular or elliptical shape of an impact basin[9]. The spatial pattern of magmatic-tectonic structures bounding Procellarum is consistent with their formation in response to thermal stresses produced by the differential cooling of the province relative to its surroundings, coupled with magmatic activity driven by the greater-than-average heat flux in the region.

The Procellarum KREEP Terrane (PKT) is defined by higher than average values of the surface abundances of potassium (K), rare earth elements (REE), and phosphorus (P)[3,10] (Fig. 1). The PKT probably experienced a geodynamical history that differed from that of the rest of the Moon because of the elevated heat flow resulting from the high crustal concentrations of heat-producing elements[10–12]. The region encompasses the majority of the Moon's mare basalt provinces, including many that are not associated with known impact basins. The interpretation of the region as an impact basin was based on its distinctive composition and generally low elevation, together with the photogeological interpretation of features as fragments of circular basin rings[5–7,13]. The most prominent candidate ring structures are the mare shorelines and scarps on the western edge of Oceanus Procellarum and the northern edge of Mare Frigoris[5] (Fig. 1a; Extended Data Fig. 1). However, these arcuate segments span only a fraction of the circumference of the proposed basin, requiring much of the original topographic rim to have been later destroyed or modified beyond recognition.

In this study, we use data from NASA's GRAIL mission[8] to examine the subsurface structure of the Procellarum region. Bouguer gravity anomalies (the free-air gravity field corrected for the contributions of surface topography) and gravity gradients (the second horizontal derivatives of the Bouguer potential[14]) reveal a distinctive pattern of anomalies surrounding the region (Fig. 1c, d). These narrow belts of negative gravity gradients and positive gravity anomalies indicate narrow zones of positive density contrast in the subsurface. Previous analyses of the GRAIL data revealed a global population of narrow, randomly oriented, ancient igneous intrusions that lack surface expressions[14]. In contrast, the PKT border anomalies are broader features that are spatially associated with the maria and appear to be part of an organized large-scale structure. These anomalies are the dominant features not associated with impact basins in the global gravity gradients, but only a portion of the western border anomalies in Oceanus Procellarum were noted in earlier gravity studies[15].

To investigate the source of the anomalies, we first inverted the gravity field in the spherical harmonic domain under the assumption that the anomalies arise from variations in the thickness of both the maria and the underlying feldspathic crust that serves as the basement of the maria (see Methods for details). We focus here on two models to illustrate the range of solutions: the first imposes an isostatic condition on the pre-mare crust, and the second forces the amplitude of the relief along the mare–basement and crust–mantle interfaces to be equal and opposite in magnitude. For these two models, the average structures across two of the border anomalies at the northwest corner of the PKT suggest the presence of elongated mare-filled depressions in the feldspathic crust having widths of $\sim$150 km and depths of 2–4 km, and underlain by crust–mantle interfaces that are shallower than adjacent areas by 3–6 km (Fig. 2e–h; Extended Data Figs 2, 3). If we instead assume that the PKT border anomalies arise from igneous intrusions in the subsurface[14], inversions of the average gravity profiles across these two anomalies yield widths of 66^{+5}_{-6} and 82^{+19}_{-36} km and vertical extents of 8^{+1}_{-1} and 6^{+3}_{-1} km for intrusions with elliptical cross-sections, assumed density contrasts of 550 kg m^{-3}, and bottom depths of 25 km (Fig. 2c, d; see Methods).

The spherical harmonic inversion solutions are consistent with thickening of the maria over linear depressions formed by crustal thinning, as could occur in volcanically flooded rift valleys[16]. The branching of anomalies that make up the western border structure and the triple-junction intersections at some corners are consistent with the attributes of planetary rifts. This interpretation is also supported by the broad elongated depressions surrounding the border anomalies beneath Mare Frigoris and western Mare Tranquillitatis, and the scarps found in the highlands adjacent to some of the border anomalies[5]. The inferred crustal thinning could arise from extension of the crust by 8–18 km (Extended Data Table 1). For the intrusion models, the large widths of the inferred intrusions (greatly exceeding the vertical dimensions), and the association of the gravity anomalies with maria at the surface, suggest that dyke-like intrusions are not solely responsible for the anomalies. A combination of crustal thinning, mare thickening, and intrusion by dyke swarms provides the most likely explanation for the anomalies. The

[1]Department of Geophysics and Center for Space Resources, Colorado School of Mines, Golden, Colorado 80401, USA. [2]Department of Earth and Planetary Sciences, University of California, Santa Cruz, California 95064, USA. [3]Department of Earth, Environmental and Planetary Sciences, Brown University, Providence, Rhode Island 02912, USA. [4]Planetary Science Directorate, Southwest Research Institute, Boulder, Colorado 80302, USA. [5]Lunar and Planetary Institute, Houston, Texas 77058, USA. [6]Hawaii Institute of Geophysics and Planetology, University of Hawaii, Honolulu, Hawaii 96822, USA. [7]Department of Earth, Atmospheric, and Planetary Sciences, Purdue University, West Lafayette, Indiana 47907, USA. [8]Solar System Exploration Division, NASA Goddard Space Flight Center, Greenbelt, Maryland 20771, USA. [9]Department of Earth, Atmospheric and Planetary Sciences, Massachusetts Institute of Technology, Cambridge, Massachusetts 02139-4307, USA. [10]Department of Terrestrial Magnetism, Carnegie Institution of Washington, Washington DC 20015, USA. [11]Lamont-Doherty Earth Observatory, Columbia University, Palisades, New York 10964, USA.

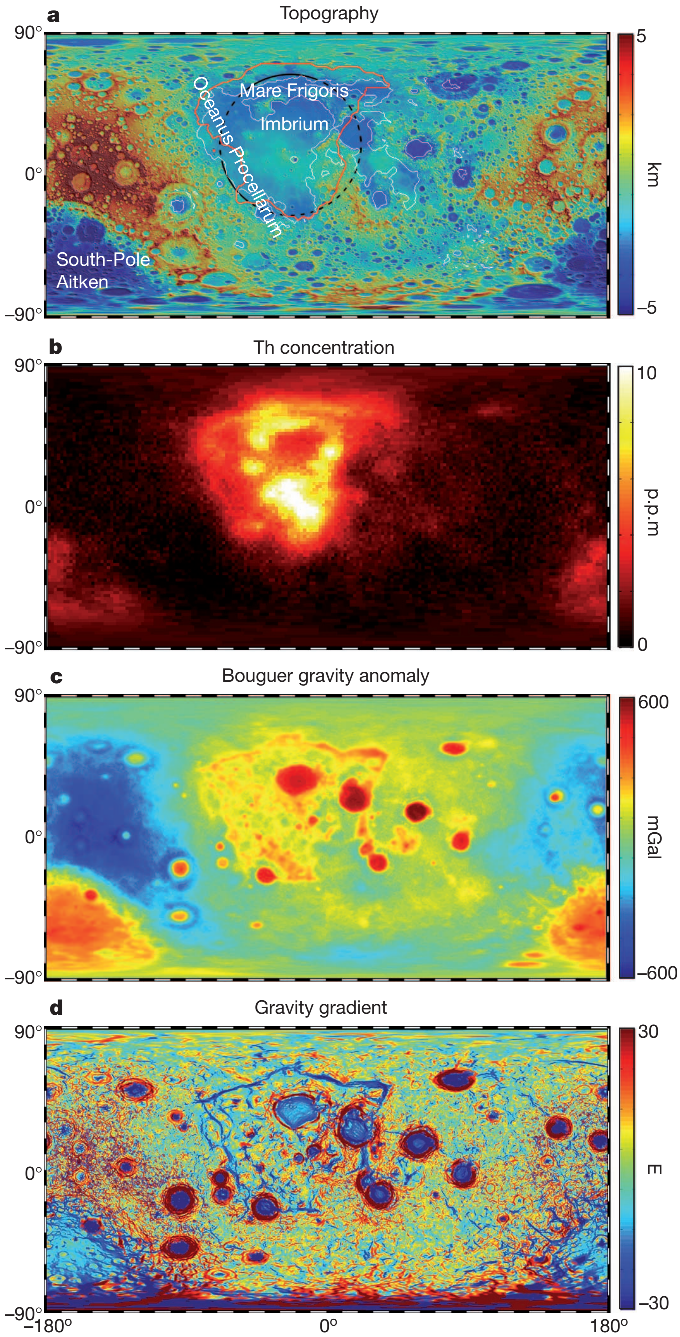

Figure 1 | Global maps of lunar properties. **a**, Topography; **b**, Th concentration; **c**, Bouguer gravity anomaly; and **d**, gravity gradient (in units of Eötvös; $1\,\mathrm{E} = 10^{-9}\,\mathrm{s}^{-2}$). All maps are simple cylindrical projections centred on the nearside. The circular rim of the proposed Procellarum impact basin[5] (black dashed line), the outline of the maria (white lines[17]), and the extent of the PKT (red line, corresponding to a Th concentration of 3.5 p.p.m.; ref. 4) are shown in **a**. Features discussed in the text are labelled in **a**.

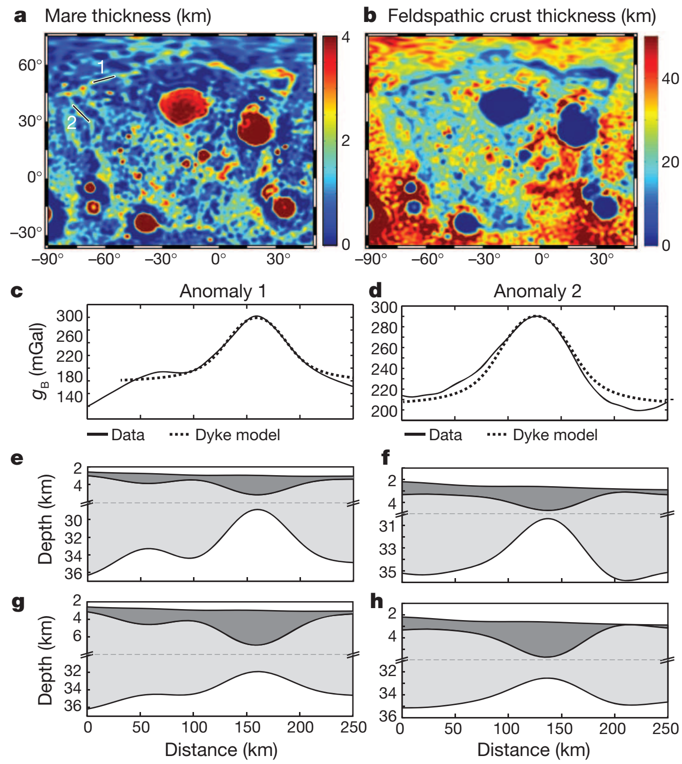

Figure 2 | Gravity and subsurface structure of the PKT border structures. **a**, **b**, Maps of the modelled thickness of the maria (**a**) and underlying feldspathic crust (**b**) assuming that the mare–basement and crust–mantle interfaces were in isostatic equilibrium before infilling by mare basalt. **c**, **d**, Profiles of the average Bouguer gravity anomaly g_B perpendicular to border anomalies 1 (**c**) and 2 (**d**); see **a** for locations. The dashed lines show the predicted gravity for the best-fit dykes. **e–h**, Average cross-sections of the model results orthogonal to border anomalies 1 (**e**, **g**) and 2 (**f**, **h**) showing the mare (dark grey) and feldspathic crust (light grey) for two different sets of filters. The filters used in the models in **e** and **f** impose the isostatic condition as in **a** and **b**, whereas the filters used in the models in **g** and **h** impose the condition that the relief along the interfaces was equal and opposite in amplitude (see Methods for further details and Extended Data Fig. 3 for results from additional models).

elevated heat flux in the PKT[10] coupled with passive mantle upwelling during rifting would have led to widespread partial melting of the underlying mantle[16], so tectonic extension would have been accompanied by dyke intrusion and volcanism. These dykes may represent the magma plumbing system that provided conduits connecting deep magma reservoirs to many of the nearside maria.

The PKT border structures are the only known lunar structures consistent with large-scale rifting of the crust, a process that is more common on Earth, Venus, and Mars. The surface exposures of the maria overlying the border structures formed 3.51 ± 0.25 billion years ago (Gyr ago; area-weighted mean and standard deviation)[17], representing the final stages of the volcanic infilling of the structures. In contrast, the rest of the nearside maria exhibit a range of surface ages of 1.2–4.0 Gyr. Volcanic infilling of the rifts may have been a self-limiting process because the flexural response to the loading would have caused compression in the upper lithosphere, possibly closing off the magma conduits. This inference is supported by the observation of wrinkle ridges overlying and parallel to the border structures. Parallel wrinkle ridges flanking the Mare Frigoris border structure may also reflect structural control of the wrinkle ridges by buried tectonic structures.

In a polar projection centred on the PKT, the border structures delineate a quasi-rectangular shape ~2,600 km in width (Fig. 3). The arcuate scarps at the edges of Mare Frigoris and Oceanus Procellarum that were previously interpreted as rim segments of a Procellarum basin are seen in the GRAIL data to be a small fraction of this continuous set of well-expressed structures that trace out a polygonal pattern consisting of predominantly straight sides and angular intersections (Extended Data Fig. 1). The northeast and northwest corners of the structure deviate from the proposed circular rim[5] by ~215 km and ~175 km, respectively. Only the discontinuous and poorly expressed anomalies in the southwestern portion of the region are compatible with a circular rim. This quasi-rectangular pattern is in contrast with the circular or elliptical shapes of all other large impact basins[9], including the ancient hemisphere-scale Borealis basin on Mars, for which a continuous elliptical basin rim can be traced in topography and gravity data[18]. The interpretation of

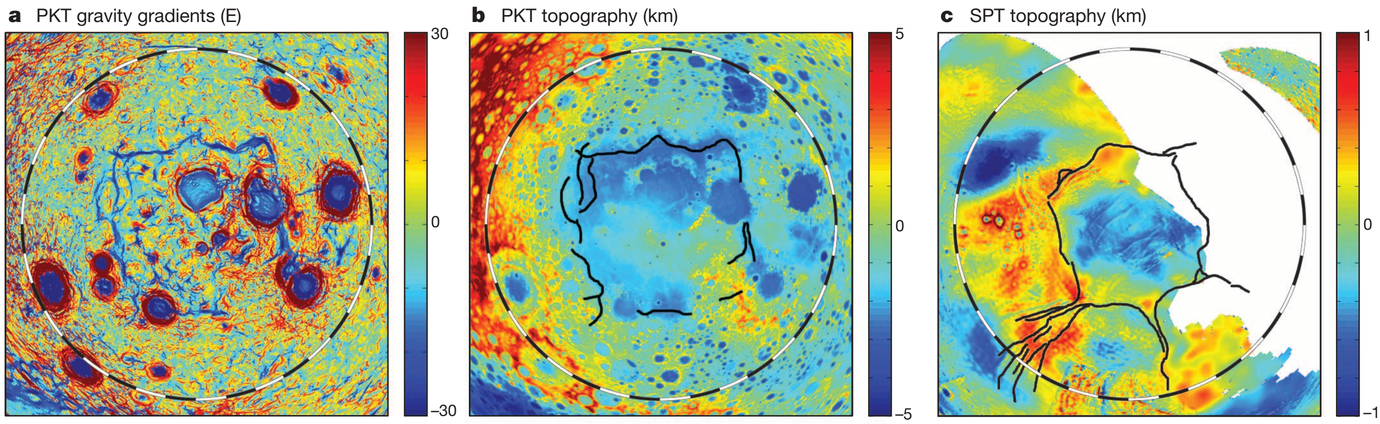

Figure 3 | Geometric pattern of the PKT border structures, with a comparison to the Enceladus SPT. **a**, **b**, The border structures of the PKT highlighted by the gravity gradients (**a**) trace out a quasi-rectangular pattern, enclosing a broad region of low elevations[1] (**b**). **c**, The SPT is similarly a region of low elevation[25] (white regions denote topography data gaps) and high heat flow[26] (Extended Data Fig. 8) surrounded by a quasi-rectangular pattern of border structures. The black lines in **b** and **c** trace the border structures surrounding the PKT and SPT, respectively. All maps are in a simple polar projection; in all panels, the circle corresponds to an angular diameter of 180° of surface arc, divided into 10° increments.

the PKT border structures as the rim of an impact basin would require hundreds of kilometres of horizontal deformation with large strain gradients to produce the angular corners, but there is no evidence for such large-magnitude strain on the Moon[19]. Furthermore, the negative gravity gradients of the border structures do not match the signatures of known impact basins, such as the Imbrium and South Pole-Aitken basins, which are characterized by paired positive and negative gradients of equal amplitude flanking the rims and negative gradients throughout the basin interiors. Although it is not possible to disprove the existence of an ancient degraded Procellarum basin that lacks a clear geophysical signature, the geometry and gravitational signature of the structures bordering the PKT do not support the interpretation that they mark the rim of a basin.

The formation and geometric pattern of the PKT border structures require an explanation. Although the gravity anomalies are consistent with either lava-flooded rift valleys or dense swarms of dykes, both interpretations require substantial extension across the border structures. The locations of the structures at the edge of the PKT suggest that the elevated heat flux in this region[10] may have played a role in the extension inferred from the gravity modelling. In a state of thermal equilibrium, both the temperature and the rate of change in temperature at a given depth in the lithosphere would be linearly proportional to the concentration of heat-producing elements in and/or beneath the crust. Thus, although the PKT was always warmer than its surroundings owing to the high concentrations of heat-producing elements, it would have cooled at a greater rate as a result of the declining radiogenic heat production[10]. The cooling lithosphere would then have experienced thermal contraction, which in turn would have caused horizontal extension at the margins. Cooling by 600 K across a region 2,000 km wide would have induced the equivalent of ~8 km of extension. We tested this hypothesis with a simple model of the thermal evolution and resultant stresses (see Methods). A finite difference model was used to represent the conductive thermal evolution of the Moon, given the equivalent of 10 km of KREEP basalt at the base of a 40-km-thick crust within a spherical cap 2,000 km in diameter[10,11]. The model predicts a temperature decrease beneath the PKT relative to its surroundings of as much as 600 K between 4.0 and 3.0 Gyr ago, with the maximum cooling at the base of the crust (Fig. 4a; Extended Data Figs 4, 5).

The stresses resulting from the thermal contraction of the lithosphere between 4.0 and 3.0 Gyr ago were calculated with an elastic finite element model[20]. The far-field stresses on the opposite side of the Moon were subtracted in order to isolate the effects of the PKT, because the mean stress in the lithosphere may have been affected by global contraction or expansion[14,21]. Cooling and contraction of the lower lithosphere within the PKT caused extension, which induced compression in the elastically coupled upper lithosphere inside the PKT, and extension throughout the lithosphere at the edge of the PKT (Fig. 4c). Similar results were obtained if the KREEP-rich material was distributed throughout the crust (Extended Data Figs 6, 7). This extension may have been augmented by an early period of global expansion[14].

Many of the maria not associated with unambiguous impact basins are found over the PKT border structures, including maria Nubium, Procellarum, Frigoris, Mortis, Somniorum, and Tranquillitatis. Rise of magma to the surface in dykes requires that the greatest tensile stress be horizontal, and a vertical gradient in stress that is conducive to magma ascent[22]. The model predicts that the extensional zone bordering the PKT was conducive to magma ascent in dykes (Fig. 4d). In contrast, horizontal compressional stresses in the upper lithosphere within the centre of the PKT would tend to inhibit the rise of magma, except where this stress field was modified by later processes such as impacts or loading and flexure of the lithosphere, or where magma ascent was aided by volatile exsolution or a pressurized magma chamber.

In order to form the observed rectilinear pattern of structures, it is necessary to break the azimuthal symmetry assumed in the model. Volumetric contraction beneath a free surface generates fracture patterns with characteristic corner angles of 120°. This pattern results in six-sided polygons at scales ranging from 1–100 cm (for example, mud cracks, columnar joints in basalt), to 1–100 m (for example, thermal contraction polygons in permafrost), to 10 km (for example, polygons from sediment compaction in the lowlands of Mars[23]). However, as the size of the structure becomes large relative to the radius of the planetary body, surface curvature becomes important. A polygon with 120° corner angles will have five or four sides when the lengths of the sides reach 41.8° or 70.5° of arc, respectively. The mean length of the PKT border structures is 2,150 km or 71°, and the angles of the vertices range from 109° to 125°. Thus, at the scale of the PKT, a set of linear rifts intersecting at 120°-angle junctions around a contracting cap may result in a quasi-rectangular structure.

We note a similarity in the pattern of structures to the south polar terrain (SPT) of Saturn's icy moon Enceladus (Fig. 3; Extended Data Fig. 8)[24,25]. Both the PKT and SPT are bordered by quasi-rectangular sets of tectonic belts with angular intersections that sometimes take the form of triple junctions. Both structures enclose regions approximately 70–80° in diameter of low topography[1,25], enhanced volcanic activity[10,24], and strongly elevated heat flow[10,26]. However, we emphasize that there are important differences between the specific processes at work and the evolutionary histories of these two different terrains, including (on Enceladus) the tidal source of the heat, the prevalence of compressional

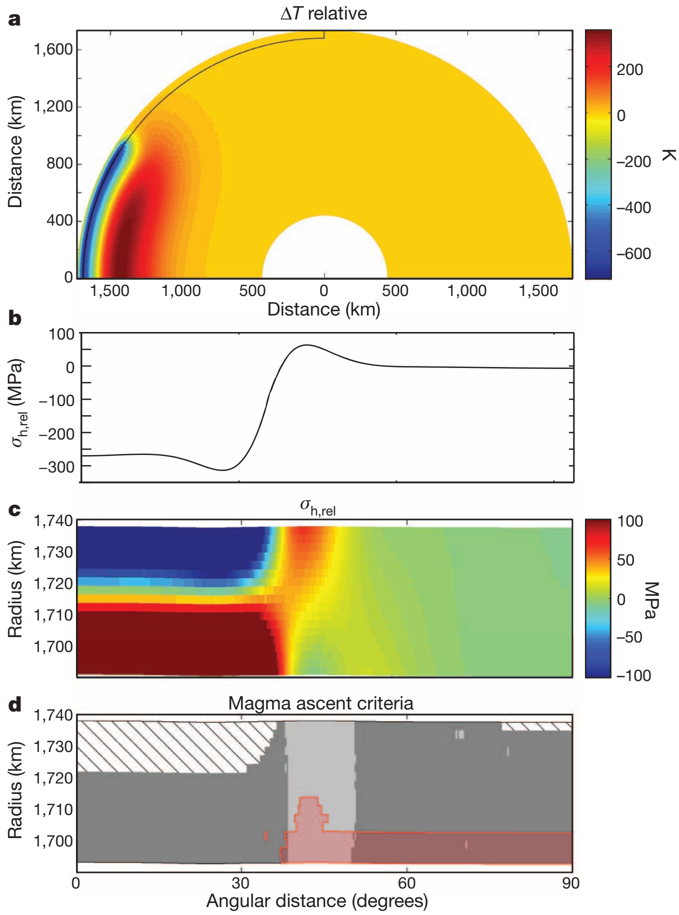

Figure 4 | Predicted temperature and stress for the Procellarum region. **a**, Predicted temperature change of the PKT relative to its surroundings between 4.0 and 3.0 Gyr ago. The Procellarum region is centred on the pole on the left side of the figure. The black line denotes the area expanded in **c** and **d**. **b**, In-plane horizontal elastic relative stress radial to the centre of the PKT at the surface predicted by the finite element model (where positive stresses are tensile; the far-field stress profile has been subtracted to calculate the relative stresses). **c**, Cross-section of the in-plane horizontal elastic relative stress. **d**, Predicted zones of magma ascent; dark grey indicates horizontal extension conducive to vertical dyke formation, light grey indicates both horizontal extension and a vertical stress gradient more favourable to magma ascent than in the lithosphere far from the PKT, and red indicates areas in which magma will rise unassisted by other factors. Cross-hatching indicates regions in which none of the criteria for magma ascent are met. The temperatures in **a** and stresses in **b**, **c** are both taken relative to the far-field values in the opposite hemisphere.

tectonics[24,25], the likelihood of a subsurface ocean[27], and the possibility of a mobile lithosphere[28]. Nevertheless, the gross morphological and geophysical similarities between the PKT on the Moon and the SPT on Enceladus suggest the possibility of broad parallels in their geodynamic evolution, and that similar parallels may exist with other magmatic-tectonic centres (for example, the northern lowlands of Mercury, an irregular depression ~80° in diameter[29] that has experienced widespread volcanic resurfacing[30]).

Online Content Methods, along with any additional Extended Data display items and Source Data, are available in the online version of the paper; references unique to these sections appear only in the online paper.

Received 18 January; accepted 16 July 2014.

1. Smith, D. E. *et al.* Initial observations from the Lunar Orbiter Laser Altimeter (LOLA). *Geophys. Res. Lett.* **37,** L18204 (2010).
2. Wieczorek, M. A. *et al.* The crust of the Moon as seen by GRAIL. *Science* **339,** 671–675 (2013).
3. Jolliff, B. L. *et al.* Major lunar crustal terranes: surface expressions and crust-mantle origins. *J. Geophys. Res.* **105,** 4197–4216 (2000).
4. Lawrence, D. J. *et al.* Global elemental maps of the Moon: the Lunar Prospector gamma-ray spectrometer. *Science* **281,** 1484–1489 (1998).
5. Whitaker, E. A. The lunar Procellarum basin. *Lunar Planet. Sci.* **12A,** 105–111 (1981).
6. Cadogan, P. H. Oldest and largest lunar basin? *Nature* **250,** 315–316 (1974).
7. Wilhelms, D. E. The geological history of the Moon. *US Geol. Surv. Prof. Pap.* **1348,** 1–302 (1987).
8. Zuber, M. T. *et al.* Gravity field of the Moon from the Gravity Recovery and Interior Laboratory (GRAIL) mission. *Science* **339,** 668–671 (2013).
9. Andrews-Hanna, J. C. & Zuber, M. T. in *Large Meteorite Impacts and Planetary Evolution IV* (eds Gibson, R. L. & Reimold, W. U.) 1–13 (Special Paper 465, Geological Society of America, 2010).
10. Wieczorek, M. A. & Phillips, R. J. The "Procellarum KREEP Terrane": implications for mare volcanism and lunar evolution. *J. Geophys. Res.* **105,** 20417–20430 (2000).
11. Grimm, R. E. Geophysical constraints on the lunar Procellarum KREEP Terrane. *J. Geophys. Res. Planets* **118,** 768–777 (2013).
12. Laneuville, M., Wieczorek, M. A., Breuer, D. & Tosi, N. Asymmetric thermal evolution of the Moon. *J. Geophys. Res. Planets* **118,** 1435–1452 (2013).
13. Nakamura, R. *et al.* Compositional evidence for an impact origin of the Moon's Procellarum basin. *Nature Geosci.* **5,** 775–778 (2012).
14. Andrews-Hanna, J. C. *et al.* Ancient igneous intrusions and early expansion of the Moon revealed by GRAIL gravity gradiometry. *Science* **339,** 675–678 (2013).
15. Scott, D. H. The geologic significance of some lunar gravity anomalies. *Proc. Lunar Sci. Conf.* **5,** 3025–3036 (1974).
16. White, R. & McKenzie, D. Magmatism at rift zones: the generation of volcanic continental margins and flood basalts. *J. Geophys. Res.* **94,** 7685–7729 (1989).
17. Hiesinger, H. *et al.* Ages and stratigraphy of lunar mare basalts in Mare Frigoris and other nearside maria based on crater size-frequency distribution measurements. *J. Geophys. Res.* **115,** E03003 (2010).
18. Andrews-Hanna, J. C., Zuber, M. T. & Banerdt, W. B. The Borealis basin and the origin of the martian crustal dichotomy. *Nature* **453,** 1212–1215 (2008).
19. Watters, T. R. & Johnson, C. L. in *Planetary Tectonics* (eds Watters, T. R. & Schultz, R. A.) 121–182 (Cambridge Univ. Press, 2010).
20. Melosh, H. J. & Raefsky, A. The dynamical origin of subduction zone topography. *Geophys. J. R. Astron. Soc.* **60,** 333–354 (1980).
21. Solomon, S. C. The relationship between crustal tectonics and internal evolution in the Moon and Mercury. *Phys. Earth Planet. Inter.* **15,** 135–145 (1977).
22. McGovern, P. J., Rumpf, M. E. & Zimbelman, J. R. The influence of lithospheric flexure and volcano shape on magma ascent at large volcanoes on Venus. *J. Geophys. Res. Planets* **118,** 2423–2437 (2013).
23. Hiesinger, H. & Head, J. W. Characteristics and origin of polygonal terrain in southern Utopia Planitia, Mars: results from Mars Orbiter Laser Altimeter and Mars Orbiter Camera data. *J. Geophys. Res.* **105,** 11999–12022 (2000).
24. Porco, C. C. *et al.* Cassini observed the active south pole of Enceladus. *Science* **311,** 1393–1401 (2006).
25. Schenk, P. M. & McKinnon, W. B. One-hundred-km-scale basins on Enceladus: evidence for an active ice shell. *Geophys. Res. Lett.* **36,** L16202 (2009).
26. Howett, C. J. A., Spencer, J. R., Pearl, J. & Segura, M. High heat flow from Enceladus' south polar region measured using 10–600 cm^{-1} Cassini/CIRS data. *J. Geophys. Res.* **116,** E03003 (2011).
27. Běhounková, M., Tobie, G., Choblet, G. & Cadek, O. Tidally-induced melting events as the origin of south-pole activity on Enceladus. *Icarus* **219,** 655–664 (2012).
28. O'Neil, C. & Nimmo, F. The role of episodic overturn in generating the surface geology and heat flow on Enceladus. *Nature Geosci.* **3,** 88–91 (2010).
29. Zuber, M. T. *et al.* Topography of the northern hemisphere of Mercury from MESSENGER laser altimetry. *Science* **336,** 217–220 (2012).
30. Head, J. W. *et al.* Flood volcanism in the northern high latitudes of Mercury revealed by MESSENGER. *Science* **333,** 1853–1856 (2011).

Acknowledgements The GRAIL mission is a component of the NASA Discovery Program and is performed under contract to the Massachusetts Institute of Technology and the Jet Propulsion Laboratory, California Institute of Technology. J.C.A.-H. was supported by grant NNX12AL20G from NASA's GRAIL Guest Scientist Program.

Author Contributions J.C.A.-H. performed the data analyses and modelling. M.T.Z. is the principal investigator of the GRAIL mission. All authors contributed to the interpretation of the results and their implications.

Author Information Reprints and permissions information is available at www.nature.com/reprints. The authors declare no competing financial interests. Readers are welcome to comment on the online version of the paper. Correspondence and requests for materials should be addressed to J.C.A.-H. (jcahanna@mines.edu).

METHODS

Gravity gradients. The gravity data analysed here were taken from gravity model GRGM900b, obtained from observations during GRAIL's primary and extended missions[31]. The Bouguer gravity anomaly model was generated for an assumed a crustal density of 2,550 kg m^{-3} (ref. 2). The Bouguer gravity gradients were calculated in the spherical harmonic domain[32] using the software archive SHTOOLS (freely available on-line at http://shtools.ipgp.fr). The eigenvalues of the horizontal gravity gradient tensor (Γ_{11}, Γ_{22}), representing the values of the maximum and minimum curvature of the potential field at each point, were then calculated. As was done previously[14], the eigenvalues were combined into a single value (the maximum-amplitude horizontal gradient, or Γ_{hh}) representing the second horizontal derivative of maximum amplitude at each point on the surface:

$$\Gamma_{hh} = \begin{vmatrix} \Gamma_{11} \ \text{if} |\Gamma_{11}| > |\Gamma_{22}| \\ \Gamma_{22} \ \text{if} |\Gamma_{11}| \leq |\Gamma_{22}| \end{vmatrix}$$

where $|x|$ indicates the absolute value of x. This maximum-amplitude horizontal gradient represents the gradient orthogonal to any structures that dominate the local gravity, regardless of their orientation. The gravity gradients are given in units of Eötvös (1 E = 10^{-9} s^{-2}). The gravity gradients were used to reveal the presence of discrete subsurface structures, whereas the Bouguer gravity anomaly and potential were used in all subsequent analyses.

In this representation of the gravity gradients, a positive density anomaly will produce a negative gravity gradient, whereas a step function density anomaly will produce a symmetric pair of positive and negative gravity gradients flanking the step. For this reason, the mantle uplift beneath large impact basins is expressed as an outer ring of positive gravity gradients and an inner ring of negative gravity gradients. Thus, although some of the border structures are near the edges of the overlying maria, the gravity gradient signatures are not consistent with the anomalies expected to arise from edge effects of the maria. Furthermore, the northern border anomaly is approximately centred within Mare Frigoris, and the western border structure exhibits three branches that are offset from the edge of the overlying Oceanus Procellarum by as much as 600 km. The average Bouguer gravity profiles perpendicular to the border structures reveal narrow positive Bouguer anomalies (Fig. 2c, d). The elongated negative gravity gradients and positive Bouguer gravity anomalies bordering the Procellarum KREEP Terrane (PKT) are most simply explained by elongated positive density anomalies.

In previous work focusing on narrower structures in the lunar gravity gradient field interpreted as elongated igneous intrusions or swarms of dykes, we calculated the gradients using a high-pass filter at degree and order 50, which emphasized shorter-wavelength structures[14]. The focus of the present work is on the longer-wavelength border anomalies surrounding the PKT, which have significant power at degrees less than 50. Thus, the gravity gradients were calculated between degrees 2 and 400, with a cosine-shaped taper applied between degrees 350 and 400. Two of the border anomalies in the northwest part of the region coincide with ancient igneous intrusions identified in the previous study of the short-wavelength gravity gradients[14]. However, the majority of the dyke-like structures identified in that study are narrower features that lack a surface expression and appear to be distributed randomly across the planet[14]. In contrast, the PKT border anomalies are longer-wavelength features that occur within the maria and appear to be part of a large-scale organized structure.

In order to highlight the true shape of the PKT border anomalies, the Bouguer gravity gradients were plotted in a simple polar projection, preserving the distance between each point and the origin, and thus preserving the shape of features centred on the origin. The global Bouguer gravity gradient map in cylindrical projection (Fig. 1) appears to show a pentagonal structure encompassing the PKT. However, re-projection in a polar projection centred on the region (Fig. 3a) reveals that the structure as a whole is dominantly quasi-rectangular. The pentagonal appearance in the cylindrical projection is a result of both the distortions at high latitudes in that projection and a kink in the northern border structure at its mid-point.

A previous study[5] mapped possible ring structures associated with the Procellarum basin on a Lambert azimuthal equal-area map of the nearside of the Moon. A comparison of the GRAIL gravity gradients with this map (Extended Data Fig. 1) reveals that the majority of the mare shorelines and major scarps identified in that study parallel the Procellarum border anomalies, and a substantial fraction of the wrinkle ridges overlie the border anomalies. However, the angular corners apparent in the gravity gradients are missing or rounded off in the mapped surface structures. The scarps and mare shorelines adjacent to the border anomalies are consistent with their interpretation as lava-flooded rifts, and the alignment of wrinkle ridges over the border anomalies is consistent with the flexural stresses expected to arise from the narrow loads inferred from the gravity data. The tracing of these structures on a Lambert azimuthal equal-area map, which does not preserve angles and causes significant distortions around the edges due to the nonlinear radial distance scale, contributes to the apparent circularity of the structures. This distortion is particularly prominent for the northwest corner of the PKT border structures, which occurs near the limb of the Moon where the distortion is at its greatest. Nevertheless, even in this projection the border anomalies clearly delineate a polygonal structure. A simple polar projection centred on the Procellarum region preserves the distance from the centre to all points and thus provides a more accurate depiction of shapes centred on the origin. Only the discontinuous structures in the southwest corner of the Procellarum region are consistent with a circular pattern.

Gravity inversions. Long-wavelength Bouguer gravity anomalies on the Moon are thought to arise largely from variations in the relief along the crust–mantle interface[2,33]. In contrast, because the gravitational potential of short-wavelength anomalies attenuates rapidly with elevation, most of the observed high-degree power in the Bouguer gravity must arise from density variations at depths shallower than the crust–mantle interface. At intermediate degrees, the origin of the gravity anomalies depends on the geodynamic setting. For the case of the PKT, the vast majority of the border anomalies occur beneath maria, and thus the anomalies probably arise at least in part from variations in the relief along the mare–basement interface. However, some minor branches extend off from the main border anomalies into the surrounding crust outside the maria, suggesting that at least some component of intrusive dykes and/or uplifted crust–mantle interface contributes to the anomalies. We consider both possibilities in our analysis.

The width of the gravity anomalies and their association with mare basalts at the surface suggest that the anomalies may be the result of local thickening of the maria above linear tectonic structures and/or uplift of the crust–mantle interface beneath those structures. To investigate this scenario, we inverted the gravity data in the spherical harmonic domain by downward continuing the Bouguer gravity to the appropriate radii and iteratively solving for the spherical harmonic coefficients describing the relief along the density interfaces of interest, taking into account the finite-amplitude effects of that relief[33]. This approach has been applied previously for calculating the relief along the crust–mantle interface[2,33], but here we wish to solve for the relief along both the mare–basement and crust–mantle interfaces. We first calculated the Bouguer gravity anomaly field using the density of mare basalt, since the maria comprise the top layer in our three-layer model (mare, feldspathic crust, and mantle). We adopt a mare density of $\rho_m = 3{,}150$ kg m^{-3}, based on the average of measured densities of Apollo mare samples[34]. The Bouguer anomaly was then used to calculate the relief along the mare–basement and crust–mantle interfaces.

The solution for the relief along two different subsurface density interfaces is inherently non-unique. In order to capture a range of possible solutions, we consider different filters to parse the gravity anomalies between the crust–mantle interface and the mare–basement interface. We designed a filter w_l to allow us to specify the desired ratio, f, between the relief along the crust–mantle interface and that along the mare–basement interface, taking into account the degree-dependent amplification of the gravity anomalies during their downward continuation to the mean depth of the interface of interest:

$$w_l = \frac{(R_M/R_0)^{l+2}(\rho_M - \rho_c)f}{(R_m/R_0)^{l+2}(\rho_m - \rho_c) + (R_M/R_0)^{l+2}(\rho_M - \rho_c)f}$$

where l is the spherical harmonic degree, ρ_c is the density of the feldspathic crust, ρ_M is the density of the mantle, ρ_m is the density of mare material, R_0 is the mean lunar radius (1,737.15 km; ref. 1), R_m is the mean radius of the mare–basement interface, and R_M is the mean radius of the crust–mantle interface. This filter was applied in calculating the relief along the crust–mantle interface, and the remaining Bouguer gravity was then used to calculate the relief along the mare–basement interface. We assumed densities of 2,550 kg m^{-3} and 3,220 kg m^{-3} for the porous feldspathic crust and mantle, respectively, on the basis of previous GRAIL analyses[2]. We assumed a mean radius of the crust–mantle interface of 1,697.15 km, resulting in a mean crustal thickness of 40 km, and a mean radius of the mare–basement interface of 1,736.15 km. The filters used for the models depicted in Fig. 2 are shown in Extended Data Fig. 2. The first model represents the case in which the feldspathic crust was in a state of isostasy before infilling by the mare, leading to a ratio f of $\rho_c/(\rho_M - \rho_c)$ (Extended Data Fig. 2a). In this model, isostasy is defined using the simple criterion of equal masses in adjacent columns. If some of the volcanic infilling of the structures occurred in parallel with the extensional tectonics, the resulting load would have driven added subsidence, which would have increased the ratio between the relief along the mare–basement and crust–mantle interfaces. The second model represents the case in which the relief along the two interfaces was equal and opposite in amplitude, with f taking on a value of 1 for degrees >10. However, because the long-wavelength topography of the Moon is largely isostatic, we adopted the isostatic ratio for f for degrees 1–3, with a linear transition between the isostatic and equal-amplitude values over degrees 3–10, and the equal-amplitude value from degrees 10 to 125 (Extended Data Fig. 2b). These two models serve to illustrate the range of possible solutions and the relative insensitivity of the inferred extension to the model assumptions. A low-pass cosine taper from degrees 125 to 150 was applied to all models.

The resulting models match the gravity data but do not take into account the effects of flexure, which would perturb the interface depths relative to their elevations before mare loading and thus alter the assumed pre-loading ratio between the relief along the interfaces. Although the models were applied globally, the results are not valid in areas outside the maria. Similarly, crustal thickness models that neglect the high density of the mare basalt and the possible variations in mare thickness will have errors within the maria. The mean radius of the mare–basement interface was chosen so as to bring the base of the maria within the Procellarum region below the surface over most of the observed maria. However, the modelled long-wavelength variations in the thickness of the maria are poorly constrained because of the ambiguity between the gravitational effects of variations in the relief along the mare–basement and crust–mantle interfaces. As a result, the distribution of areas with predicted mare thicknesses greater than zero only approximately matches the observed distribution of the maria. Nevertheless, the short-wavelength variations in the thickness of the maria beneath the border anomalies are robust, given the model assumptions.

The density of the lunar mantle beneath the PKT is not known. The process responsible for concentrating the KREEP-rich materials on the nearside of the Moon may have also brought dense ilmenite-rich cumulates to the base of the crust on the nearside[35]. Overturn of the buoyantly unstable magma ocean cumulates would have mixed this material to deeper levels in the lunar mantle[36,37], but this overturn may have been limited by the high viscosity of the solid ilmenite-rich cumulates and is predicted to have occurred only for a limited range of scenarios[38]. It is possible that a mixture of olivine and ilmenite-rich cumulates sank as solid diapirs, leaving behind a portion of the ilmenite-rich material at shallower levels[38]. To account for the possibility of shallow ilmenite-rich material beneath the PKT, we considered a high-mantle-density end-member model with an assumed mantle density of 3,500 kg m^{-3}, representative of the density of the late-stage crystallization products from the magma ocean[37]. The higher mantle density reduces the predicted mantle uplift beneath the border structures, and similarly reduces the predicted extension.

We also considered two additional end-member scenarios in our gravity models. For one model, we assumed that all of the gravity anomalies at degrees $>$10 arise from variations in the thickness of the maria. This model required a mean mare–basement interface radius of R_0 – 6 km in order to bring the mare–basement interface below the surface in the regions of interest. For another model, we assumed that all of the gravity anomalies at degrees $>$10 arise from variations in the relief along the crust–mantle interface. This model became unstable at higher degrees because of the amplification of the high-degree gravity anomalies during downward continuation to the mean depth of the crust–mantle interface, so a cosine taper was applied between degrees 75 and 100 to stabilize the solution. As a result, this model is a factor of 1.6 coarser in resolution than the other models. This result provides further evidence that the short-wavelength gravity anomalies must arise from density anomalies at depths more shallow than the crust–mantle boundary. This model ascribing all of the Bouguer gravity anomaly field to variations along the crust–mantle interface is comparable in resolution to the global GRAIL crustal thickness models[2] (low-pass filtered with an amplitude of 0.5 at degrees 87 and 80, respectively, corresponding to spatial wavelengths of 63 and 68 km). In contrast, the models ascribing a substantial fraction of the Bouguer gravity field to the shallower mare–basement interface are higher in resolution (low-pass filtered with an amplitude of 0.5 at degree 137, corresponding to a spatial wavelength of 40 km). For both of these models, we assumed that variations in the top and bottom surfaces of the feldspathic crust from degrees 1 to 3 were isostatically compensated before mare flooding, with a linear transition to the desired filter from degrees 3 to 10. These final two models are not likely to be accurate representations of the subsurface structure, but they bracket the range of possible solutions.

The predicted relief along the interfaces was used to calculate the thicknesses of the feldspathic crust and maria (Extended Data Fig. 3). The broad patterns of mare thickness in this region as indicated by the models are highly uncertain because of the non-uniqueness of the division of the gravity anomalies between the mare–basement and the crust–mantle interfaces. In some areas, the predicted base of the mare rises above the surface, indicating the need for subsurface mass deficits such as those that could arise from additional variations in the crustal thickness or density in order to explain the observed gravity field within the context of this model. These errors outside the maria do not affect the predictions for the Procellarum border structures. The local thickening of the mare over the western Procellarum border structure is broadly consistent with maps of the mare thickness derived from geological constraints, such as the burial depths of impact craters, which show local thickenings of up to $>$1.5 km along this structure[39]. Models combining the effects of dykes with the relief along the mare–basement and crust–mantle interfaces would predict narrower dykes than models that ascribe the entire gravity anomaly to the presence of dykes, and reduced relief along the density interfaces relative to models without dykes.

The extension across the structures was calculated from the thickness of the feldspathic crust by integrating the fractional crustal thickness anomaly across the structures:

$$\Delta L = \int_{x_1}^{x_2} \left(1 - \frac{c(x)}{c_0}\right) \mathrm{d}x$$

where ΔL is the change in length between locations x_1 and x_2, $c(x)$ is the thickness of the feldspathic crust as a function of location, and c_0 is the mean thickness of the crust on either side of the structure. The extension was calculated between the shoulders on either side of the rift for each model, encompassing a zone 131 and 152 km wide for anomalies 1 and 2, respectively. The calculated extension and corresponding extensional strain across the structures for each of the models are given in Extended Data Table 1. The models with an isostatic ratio between the relief at the top and bottom of the feldspathic crust predict greater extension because a larger fraction of the gravity signal is downward continued to the crust–mantle interface, resulting in greater amplification of the short-wavelength anomalies. The extension calculated using the crustal thickness models is an upper bound because some contribution to the gravity anomaly arising from the mechanical or thermal reduction of the crustal porosity beneath the mare load and surrounding the intruded dykes is likely.

We next inverted the Bouguer gravity over the PKT border structures for the best-fit dykes using a Monte Carlo approach. The sources of the anomalies were represented as density anomalies with elliptical cross-sections in the vertical plane perpendicular to the long axes of the anomalies, of assumed density contrast and bottom depth and unknown width and top depth. The bottom depths were set to the typical crustal thickness within the PKT of $\sim$25 km (ref. 2), and the density contrasts were set to 550 kg m^{-3}, corresponding to a crustal density of 2,550 kg m^{-3} (ref. 2) and an intrusion density of 3,100 kg m^{-3} (ref. 34). Dykes with elliptical cross-sections were then constructed from a large number of rectangular prismatic elements, and the gravity anomaly was calculated from those prisms[40]. The best-fit solutions were found using a simple Markov chain Monte Carlo (MCMC) approach[14]. The one-standard-deviation (1σ) confidence intervals on the best-fit solutions were obtained by using a Metropolis-Hastings MCMC to test 20,000 models and analysing the histograms of the resultant model parameters[14]. If the volume of the dyke is accommodated solely by horizontal extension, then the resulting extensions for anomalies 1 and 2 are 21 km and 20 km, respectively, given intrusion into a 25-km-thick crust.

Thermal modelling. The thermal evolution of the PKT was modelled following earlier work by Wieczorek and Phillips[10] and Grimm[11], under the assumption of conductive heat transfer through the mantle. The results of this work are primarily sensitive to the temperatures in the lithosphere, which are dominated by the concentration of heat-producing elements in the crust and the conductive heat transfer through the lithosphere. Although early convection beneath the PKT was possible[12], this convection would have had only a second-order effect on the temperatures in the lithosphere. We used a finite difference approach to solve the spherical axisymmetric thermal diffusion equation. The model was benchmarked against the analytic solution for half-space cooling from an instantaneous temperature change applied to the surface, as well as by comparison with the results of previous work[10]. The model nodes were divided into crust, mantle, and KREEP components.

The PKT was represented by a spherical cap 2,000 km (66°) in diameter in which the concentration of heat-producing elements was enhanced. The lack of similarly high concentrations of heat-producing elements on the farside is supported by the lack of evidence for KREEP-rich material within or surrounding the South Pole-Aitken impact basin[3]. The cause for this concentration of incompatible elements on the nearside is not known, but it may be related to a degree-1 Rayleigh–Taylor instability that arose from the gravitational instability of the dense ilmenite-rich cumulates formed in the late stages of magma ocean crystallization[35]. The crustal thickness was set to a uniform value of 40 km in order to isolate the effect of the concentration of heat-producing elements in the PKT. The effect of the thicker crust outside the PKT is less than the uncertainties in the concentration of heat-producing elements and the thermal conductivity of the crust and PKT. We assumed a thermal conductivity of 2.0 W m^{-1} K^{-1} for the crust and KREEP-rich material, and 3.0 W m^{-1} K^{-1} for the mantle. The densities of the crust/PKT and mantle were set to 2,550 and 3,200 kg m^{-3}, respectively, and a specific heat of 1,200 J kg^{-1} K^{-1} was assumed for all materials.

Previous studies favoured a 10-km-thick layer of KREEP basalt at the base of the crust[10,12], but other workers have argued that this scenario is not compatible with the gravity and topography of the region and generates too much melt[11]. In our nominal model, we included a 10-km-thick layer of KREEP basalt at the base of the crust. We also considered the case of a 10-km-thick layer of KREEP basalt distributed uniformly throughout a 40-km-thick crust. We assumed a U concentration in the KREEP basalt of 3.4 p.p.m. by weight, and concentrations of 0.14 p.p.m. and 6.8 p.p.b. in the crust and mantle, respectively[10,12]. We assumed a K/U ratio of 2,500 and a Th/U ratio of 3.7 in all materials[12]. The enhanced concentration of KREEP is given an abrupt edge in the thermal model for simplicity. The thermal effects of this edge are broadened over the thermal diffusion length scale (~50 km for 100 Myr), whereas the stress effects are spread out over a distance comparable to the flexural half-wavelength (~540 km for a lithosphere thickness of 50 km). The overall stress pattern would be unaffected by tapering the margins of the KREEP terrane over length scales of this order. The effects of melting and melt extraction on the temperature evolution were neglected. Extraction of melt would reduce the magnitude of the thermal anomaly in early time steps and decrease the amount of cooling by a modest amount, but would not change the character of the results.

High temperatures throughout the lunar interior are expected after accretion and solidification of the magma ocean[37]. The model was initialized with an approximation to an adiabatic temperature gradient throughout the model domain[10], increasing linearly from 1,450 K at the surface to 1,500 K at the core–mantle boundary at a radius of 438 km. This temperature profile represents the temperature at the end of an early convective period. In the absence of an early period of convection, the temperatures at the top of the mantle after magma ocean overturn would have been similar[37]. The top boundary condition was set to a constant temperature of 250 K, approximating the radiative equilibrium temperature of the lunar surface. A constant heat flux of 0 was applied as the basal boundary condition at the core–mantle boundary. The model begins at time $t = 0$ (4.5 Gyr ago) and was run forward in time for 4.5 Gyr. The change in temperature with time was calculated between 4.0 Gyr ago (somewhat before the onset of the geological record) and 3.0 Gyr ago, bracketing the period during which the majority of the maria formed[17,41,42]. It is only the change in temperature that generates thermal stresses in the lithosphere, so even though the PKT was always warmer than its surroundings, its time evolution was characterized by net cooling and thermal contraction because it cooled at a faster rate. The temperature change of the PKT relative to the surroundings was also calculated for illustration purposes by subtracting the temperature change profile at the antipode of the PKT. The absolute change in temperature was used in all stress modelling, but the relative temperature change serves to highlight the evolving thermal anomaly beneath the PKT.

The changes in temperature as functions of time at 25 km depth (the midplane of the 50-km-thick lithosphere assumed for the stress modelling) both within and outside the PKT are shown in Extended Data Fig. 4. Both scenarios for the distribution of KREEP-rich material show similar patterns, but the model with an isolated KREEP-rich layer beneath the crust experiences an early phase of warming in the first few hundred million years. Between 4.0 and 3.0 Gyr ago, both models predict substantially more cooling in the PKT than elsewhere. The mantle immediately below the PKT follows a similar pattern of cooling with time as a result of the decline in heat production within the PKT. In contrast, the mantle at deeper levels warms up as it slowly comes into thermal equilibrium with the overlying KREEP material[10] (Extended Data Fig. 5). However, the net effect of the cooling upper mantle and warming lower mantle approximately cancel out. The temperature changes predicted here are somewhat larger than those of Wieczorek and Phillips[10] as a result of the different ratios between the concentrations of heat-producing elements[12] and the neglect of latent heat and melt extraction effects in this study. Reducing the concentration of radiogenic isotopes or taking into account melt extraction would reduce the magnitudes of the predicted temperature changes and stresses, but would not affect their spatial patterns.

There is substantial uncertainty in the early thermal state of the Moon. The variation of temperature with depth after accretion and solidification of the magma ocean depends strongly on the timescale of accretion[43], the depth of the magma ocean[21,43], and the possible gravitational overturn of the magma ocean cumulates[37,38]. However, our models depend primarily on the temperatures within the lithosphere, which are dominated by the time evolution of the heat production within the crust. By 4.0 Gyr ago, the time at which we begin tracking the temperature changes to calculate the strain, the effect of the assumed initial condition on the temperatures in the lithosphere is greatly reduced. The early period of thermal equilibration of the lithosphere is reflected in the ~200-Myr period of increasing temperature for the case of KREEP-rich material concentrated at the base of the crust (Extended Data Fig. 4). The magnitude of this warming is substantially less than the magnitude of the cooling that follows. The possible persistence of mantle convection throughout the time period of interest[12] would affect the distribution of temperature with depth in the mantle but would have little effect on the time evolution of the temperature in the lithosphere.

Both Apollo seismic observations[44] and GRAIL gravity measurements[2] indicate that the Moon's upper crust is fractured and porous, possibly to a depth of ~20 km. This porosity is likely to reduce the thermal conductivity of the upper crust[45]. The viscous closure of porosity is a thermally activated process[2,46], so the higher temperatures within the PKT (Extended Data Fig. 4) may have decreased the crustal porosity and increased the thermal conductivity in the PKT relative to its surroundings. This increased thermal conductivity would have acted to accelerate the cooling of the PKT relative to that shown in Extended Data Figs 4 and 5. We have not attempted to model this process in detail, but we note that it will positively reinforce the thermal evolution discussed here.

Stress modelling. The stresses resulting from the changes in temperature with time were modelled using the Tekton finite element software[20] in a spherical axisymmetric geometry subject to a uniform radial gravitational acceleration. In order to provide adequate spatial resolution in the PKT, the model domain was limited to the elastic lithosphere, assumed to be 50 km thick (see discussion below). The bottom boundary condition represented the restoring force of the mantle with a pressure that varied with depth, whereas elements were free to move in both vertical and horizontal directions. The effects of the buoyant upward pressure arising from thermal anomalies in the mantle below the PKT were applied to the bottom boundary as an additional pressure term that varied with location on the basis of the thermal model results. This pressure term was calculated as the depth integral of the density contrast relative to background density, scaled by the gravitational acceleration. Although considerable thermal anomalies are predicted in the sub-lithospheric mantle beneath the PKT, the effects of the cooling upper mantle and warming lower mantle largely cancel out. The remaining pressure contributes to a broad upwarping of the surface[11] but has little effect on the short-wavelength stresses that are the focus of this analysis. The final topography and gravity anomalies over the PKT as a whole would have been strongly affected by the flexural resistance of the lithosphere[11], the thinning of the crust within the PKT[2], and loading by the maria[12]. The excess basal pressure far from the PKT, representing the effects of net global expansion or contraction, was subtracted from the basal pressure condition throughout the model. The net volume change of the interior could add a uniform compressional or extensional horizontal stress to the lithosphere, depending on the early thermal history of the Moon[14,21,43]. The model domain of a 50-km-thick lithosphere stretching from pole to pole was divided into 600 nodes in the azimuthal direction and 20 nodes in the radial direction, resulting in element dimensions of 9.1 by 2.5 km at the surface.

The predicted temperature change between 4.0 and 3.0 Gyr ago (Extended Data Fig. 5b, d) was used to calculate the resulting instantaneous elastic stresses in the model elements before any deformation[47]:

$$\sigma = \alpha_v \Delta T \frac{E}{3(1-2v)}$$

where σ is the stress (taken here to be isotropic), α_v is the volumetric coefficient of thermal expansion (assumed to be $2 \times 10^{-5}\,\mathrm{K}^{-1}$), E is Young's modulus (assumed to be 100 GPa, which is probably appropriate for the lower crust in which the greatest contraction occurs), and v is Poisson's ratio (assumed to be 0.25). These pre-strain thermal stresses were added to the lithostatic stresses for the initial condition for the finite element model. Imposing the effects of thermal contraction with the pre-strain stresses allows the resultant deformation and its effects on the stress field to arise self-consistently in the model.

The elastic stresses were calculated relative to the far-field values at the opposite side of the Moon in order to isolate the effects of thermal contraction of the PKT. Geological and geophysical evidence suggests that the net stress state of the Moon may have evolved from global expansion and extension to contraction and compression over the course of its thermal evolution[14,21]. In this scenario, the net global stress change at the time of formation of the border anomalies may have been small. However, theoretical models have shown that an early period of global expansion is difficult to generate for many likely lunar formation scenarios[43]. We put this question aside and focused instead on the local stresses within and surrounding the PKT relative to the typical stresses far from the region. These stresses would have been modified by the global stress state at the time of interest by the addition of a uniform compressional or extensional horizontal stress. In addition to the relative stresses, we also show the difference between the in-plane horizontal (that is, radial to the centre of the PKT) and vertical stresses ($\sigma_h - \sigma_v$) and the deviatoric horizontal stress ($\sigma_h - \sigma_p$), where σ_p is the pressure or mean stress value over all three directions (Extended Data Fig. 6). The width of the zone of predicted extension (~400 km) is somewhat wider than the observed border structures (~200 km), but localization of the strain would probably have occurred if the structures are analogous to lava-flooded rifts. Similar stress patterns are predicted if KREEP-rich material is distributed uniformly through the crust, though the magnitudes of the stresses are reduced (Extended Data Fig. 7) because of the reduced temperature changes (Extended Data Fig. 5c, d).

The stresses predicted by the model are dominated by the simple horizontal contractional stresses within the lithosphere. However, volumetric contraction also induces small changes to the surface topography, which generates bending stresses of small magnitude. Models in which the vertical displacement was set to zero at either the top or the bottom of the model domain resulted in similar stress fields, demonstrating that bending stresses do not contribute markedly.

The modelling in this study was intentionally simple in order to isolate the effect of the contracting cap within the PKT. This analysis did not consider the effects of spatial or temporal variations in the lithosphere thickness. Because the dominant source of stress is the horizontal contraction of the lithosphere within the PKT, the stresses for the case of a variable lithosphere should be similar. This model represented only the elastic stresses within the lithosphere. A viscoelastic model of the lithosphere and underlying mantle would predict a viscous transition zone at the base of the lithosphere within which the stresses decreased to zero at depth. Coupling of the thermal and viscoelastic evolution would result in a lithosphere that thickens with time, and would probably reduce the magnitude of the predicted extension, but would not change the character of the results. Within the PKT, the stresses are characterized by compression in the upper lithosphere and extension in the lower lithosphere, whereas at the edges of the PKT the extensional stress reaches the surface. However, the frictional strength at the surface should approach 0 MPa, allowing release of the shallow compressional stresses. Brittle compressional failure of the frictionally weak upper lithosphere throughout the PKT would allow further contraction of the spherical cap, substantially enhancing the extension at its margins.

In order to model directly the formation of the observed border structures, it would be necessary to localize the extension through tectonic failure. The localization of the extensional failure at discrete rift zones in the border structures would be dependent on the strain rate, rheology, and crustal thickness[48]. Failure at the edges of the PKT would relieve the stresses in the interior and allow the spherical cap to pull away from the surrounding lithosphere. Future work is needed to model more directly the formation of these border structures. In this work, we simply show that thermal contraction of the PKT predicts extension at its edges, providing a straightforward mechanism for generating the PKT border structures. Additional stresses arising from uplift or subsidence of the lithosphere[11,12] and magmatic processes would have also probably played a role.

Zones favourable to the ascent of magma-filled dykes through the lithosphere were identified as those experiencing in-plane horizontal extension relative to the vertical stress and a favourable vertical stress gradient. Horizontal extension is required for the formation of vertical dykes, which would otherwise flatten out to produce horizontal sills. In addition, the upward propagation of the dykes requires that the vertical gradient in the confining horizontal stress in the lithosphere ($d\sigma_h/dz$, where positive stresses are tensile, z is positive upward, and σ_h includes both the lithostatic stress and the added tectonic stress) be greater than the hydrostatic pressure gradient in the magma, causing the lower tip of the dyke to pinch shut as the upper tip propagates upward. The low density of the lunar crust[2] is an impediment to the rise of magma, even in a neutral stress state. Magma ascent is favoured in cases in which the upper lithosphere is in a state of extension relative to the lower lithosphere[49]. For a magma density of 2,900 kg m^{-3}, this state corresponds to a vertical gradient in the horizontal stress in the lithosphere in excess of 4.7 MPa km^{-1}. However, the stress gradient in the upper portions of a conductively cooling lithosphere with internal heat production and basal heating is generally not conducive to magma ascent as a result of the increasing horizontal extension with depth caused by the declining thermal gradient in the lithosphere with time. This problem could be ameliorated by a failure-induced reduction in the extensional stresses in the lower crust, by volatile exsolution within the magma to enhance the driving force for magma ascent[50], or by a pressurized magma reservoir at depth. We use the criterion of a vertical stress gradient >4.7 MPa km^{-1} for unassisted magma rise, and we also look at the stress gradient relative to the far-field value antipodal to the PKT to assess the relative tendency for magma to rise through the lithosphere if assisted by other factors as discussed above.

By these criteria, the zone at the margin of the PKT experiences stresses most conducive to magma ascent and eruption. Extensional horizontal stresses radial to the centre of the PKT would facilitate the formation of circumferential dykes throughout the full vertical extent of the lithosphere. The stress gradient in this zone is more conducive to magma ascent than anywhere else on the Moon. For the case of heating by a layer of KREEP at the base of the crust, magma would be predicted to rise unassisted to the middle of the lithosphere, whereas further ascent would require additional driving forces (Extended Data Fig. 6c). For the case of heating by KREEP distributed throughout the crust, the zone at the edge of the PKT is still the preferred location of magma ascent, but some added driving force such as volatile exsolution or a pressurized magma chamber is required for the rise of magma into the crust (Extended Data Fig. 7c).

The model also predicts changes to the surface topography. The thermal contraction of the lithosphere with time causes surface subsidence due to the vertical component of that contraction. Additionally, the horizontal shortening of the spherical cap centred on the PKT results in further subsidence because the decrease in the area of the cap must be accommodated by an increase in the radius of curvature, resulting in a decrease in elevation. Taking into account both the thermal contraction of the lithospheric cap in the PKT and the effects of thermal anomalies in the mantle, our models predict changes in surface topography less than 0.5 km during the period between 4.0 and 3.0 Gyr ago. This result cannot be directly compared with the observed topography because it represents only the change in topography over a fraction of lunar history. However, we note that the predicted elevation changes are smaller than the observed relief. The topographic depression within Procellarum cannot be explained by thermal subsidence alone.

Previous work indicated that the patterns of uplift predicted by thermal models of the PKT are difficult to reconcile with the observed long-wavelength gravity and topography[11,12]. However, the gravity and topography within the PKT are also probably affected by variations in the thickness of the crust and by possible density anomalies in the underlying mantle[12]. The low topography within the PKT may also be affected by a reduction in the porosity of the crust from thermal annealing[46]. For a lunar crustal porosity of 12% (ref. 2), annealing the pore space in the lower 10–20 km would reduce the surface elevation by 1.2–2.4 km, consistent with the observed relief.

Geometry of the PKT border structures. In order to understand the shape of the observed pattern of border structures in a spherical geometry, we used the spherical law of cosines to determine the vertex angle θ for a regular polygon on the surface of a sphere, with n sides of angular length s (in radians):

$$\theta = 2\arccos\left(\frac{\cos(h) - \cos(h)\cos(s)}{\sin(h)\sin(s)}\right)$$

where h is the angular length of the path from the polygon centre to the vertex, given by:

$$h = \arcsin\left(\sqrt{\frac{\cos(s)-1}{\cos(2\pi/n)-1}}\right)$$

These equations were used to calculate the side length at which a regular polygon with 120° vertices will have either four or five sides, rather than the six-sided figure expected for a flat Euclidean geometry.

We suggest that the quasi-rectangular pattern of border structures surrounding the PKT is consistent with the intersection of linear rifts at 120°-angle triple junctions when the effect of the curvature of the surface is taken into account. Although the PKT border structures display some intermediate kinks and intersections, the overall pattern is quasi-rectangular. Similarly, although small-scale contraction-crack polygons of all types in nature often have highly irregular forms, in the absence of competing effects (such as progressive subdivision of the polygons) the average structure is hexagonal because of the dominance of 120°-angle triple junctions at the vertices[51]. At small scales, the diameter of the polygons is determined by the size of the stress shadow around the fractures, which is proportional to the depth to which the fractures propagate[51]. The depth of fracturing for small contraction-crack polygons on Earth is dictated by the strain rate, the variation of stress with depth, and the rheology of the material in which the fractures form[51]. For the PKT, the size of the polygon was probably determined instead by the diameter of the tensile stress belt at the surface surrounding the thermal anomaly. The propagation of the fractures or rifts into the interior of the region may have been prevented by the compressional stresses in the upper lithosphere above the thermal anomaly (Extended Data Figs 6, 7), which may have had an effect similar to the stress shadows around fractures in small-scale polygons. Although the analogy of the quasi-rectangular pattern of border structures to smaller polygonal fracture patterns provides a simple explanation for the observed geometry, further testing of this hypothesis will require consideration of the competing effects of the regional stress directions, the stress field generated by the structures themselves, and the concentration of stress at the tips of the propagating faults or dykes. An alternative explanation for the pattern of border structures that warrants further consideration is that the distribution of KREEP-rich material in the subsurface may follow a quasi-rectangular pattern. However, the distribution of KREEP-rich material in the subsurface is poorly constrained, and the distribution on the surface is strongly affected by the ejecta of the Imbrium basin and the distribution of KREEP-rich maria (which was controlled in part by the pattern of the PKT border structures).

Parallels between the PKT and the south polar terrain of Enceladus. The overall pattern of the PKT border structures bears a strong resemblance to that of the border structures surrounding the south polar terrain (SPT) of Saturn's icy moon Enceladus, which are also quasi-rectangular in outline[25]. However, as discussed in the main text and expanded upon below, substantial differences exist between these provinces and their inferred evolutionary histories. We emphasize that we do not suggest that the specific processes and evolutionary paths of these two regions were identical. Rather, the gross similarities between these two provinces on different bodies suggests broad parallels in the processes governing their evolution. Here we summarize the basic properties of each province, and then discuss the SPT in more detail.

The PKT on the Moon is a broad area of enhanced surface heat flow as a result of the high concentrations of heat-producing elements within the KREEP-rich material[3,10] (Extended Data Fig. 8). This compositional anomaly is probably a result of the concentration beneath the nearside of the late-stage crystallization products of the lunar magma ocean[35], including dense ilmenite-rich cumulates and KREEP-rich material with high concentrations of U, Th, and K. The PKT was the most volcanically active region on the Moon and contains the majority of the mare basalt provinces[10]. GRAIL gravity anomalies and gradients indicate that the PKT is surrounded by a quasi-rectangular set of magmatic-tectonic structures with straight sides and angular intersections. The border anomalies along the northern (Mare Frigoris) and eastern edges of the PKT occur beneath maria that are confined within elongated topographic depressions, whereas the border anomalies on the western and southern edges of the PKT lie adjacent and interior to the topographic step up to the highlands. The PKT is characterized by low topography that is largely isostatically compensated at long wavelengths. This compensated depression can be explained by a crust that is thinner[2] or denser than that of surrounding areas, by the presence of denser materials at depth, or by a combination of these effects. Thermal annealing of the pore space beneath the PKT due to its high heat flow may have increased the bulk density of the crust at depth, which may contribute to the low topography[46]. Deeper density anomalies could result from either the intrusion of KREEP-rich magma into the lower crust, or from the presence of a remnant of the ilmenite-rich cumulates in the upper mantle that may not have fully mixed into the deeper interior[38]. Although a thinner crust probably explains most of the observed topography, contributions from reduced crustal porosity and the presence of dense materials within or below the crust appear likely.

The SPT on Enceladus is an area of strongly enhanced surface heat flow[26,52,53] (Extended Data Fig. 8) as a result of either localized tidal heating or the localized release of global tidal heating. The source of this thermal anomaly is thought to be related to the presence of a regional liquid water sea or the regional thickening of a global ocean beneath the SPT, which may be a result of locally enhanced tidal heating and would itself contribute to the enhanced tidal heating[27,54,55]. The SPT is cyrovolcanically active, as revealed by the plume of water vapour and icy particles emanating from the parallel 'tiger stripes' fractures in the centre of the SPT[24]. Cassini Imaging Science Subsystem (ISS) images reveal the SPT to be bounded by a quasi-rectangular set of tectonic structures with straight sides and angular intersections[24]. These border structures occur near the edges of the topographic depression containing the SPT[24], located either at or just above the topographic step leading from the SPT up to the surrounding surface[25] (Fig. 3c). The SPT is characterized by low topography[25,56] that is largely isostatically compensated at long wavelengths[57], which is best explained by the presence of a relatively dense subsurface ocean[57,58]. Depressions in other areas of Enceladus[25] have been explained as resulting from the thermal annealing of the pore space due to the presence of local thermal anomalies beneath these regions in the past[59]. Some contribution to the SPT depression from a reduction of the pore space seems probable given the high observed heat flow. However, the large apparent depth of compensation of the SPT indicated by the long-wavelength gravity and topography suggests that the effect of a deeper ocean dominates[57].

Although there are notable large-scale morphological and geodynamic similarities between the PKT and the SPT, there are many differences between these provinces as well. The thermal anomaly in the SPT is a result of tidal, rather than radiogenic, heating. Multiple mechanisms have been proposed to explain the high heat flux in the SPT, including viscous heating in the ice shell[55] and shear heating along fractures[60]. Each of these mechanisms ultimately relies on tidal energy from the gravitational interaction of Enceladus with Saturn. However, the expected steady-state rate of tidal heating for the present-day eccentricity[61] is not sufficient to maintain the observed heat flux within the SPT[26,53] or the inferred subsurface ocean beneath the region[27]. Recent results have revised the lower bounds on the heat flow downward[52], but values remain above the expected steady-state tidal heating unless the dissipation within Saturn is higher than expected from theoretical considerations[62]. This discrepancy may be explained if the SPT today is in a transient state of high heat flow following an earlier period of high orbital eccentricity during which the ocean formed[27]. This scenario implies a time-variable heat flux in which the SPT may be cooling today.

The lack of craters within the SPT[24] suggests an earlier episode of volcanic resurfacing, lithosphere recycling[28,63], or viscous relaxation of the craters[64]. Each of these scenarios could have resulted in a regional thermal anomaly, followed by a period of cooling and contraction of the ice throughout the SPT. Globally, substantial lateral and temporal variations in the heat flux have been inferred on the basis of high local heat fluxes indicated by the relaxation of craters[64] and the flexural support of topography[65]. Structures similar in scale and morphology to the SPT on the leading and trailing hemispheres suggest similar activity at those locations in the past[66], further supporting spatial and temporal variability in the thermal state of Enceladus's ice shell.

The SPT border structures are each composed of a belt of closely spaced parallel ridges, surrounded by an inward (southward) facing scarp[24,67]. The ridge belts probably formed by compression[24,25], though extensional deformation[68] or more complicated scenarios[69] may have played a role in the formation of the south-facing scarps. For the compressional interpretation, it has been proposed that the tectonics in the SPT was driven by regional thermal expansion[70], which is similar in nature but opposite in sign to what is proposed here for the PKT. At some intersections, the border scarps are continuous with fracture belts extending northward from 120°-angle triple junctions[67], consistent with an extensional origin for the outer scarp. However, the folded terrains confined within the angular corners are indicative of compressional deformation[24]. Compressional folding is also observed in the interior of the SPT away from the border structures[71], whereas tensile opening of the 'tiger stripe' fractures is required to explain the observed volcanic venting[72]. Thus, both compressional and extensional tectonics have been active along the border structures and within the interior of the SPT.

Some structures observed within the SPT are broadly consistent with our model predictions for the PKT. The models predict the upper lithosphere within a cooling lithospheric cap to be in a state of compression due to its coupling with the contracting lower lithosphere, whereas the cap would be surrounded by a belt in which extensional stresses pervade the entire lithosphere (Fig. 4, Extended Data Figs 6, 7). This stress pattern predicts broad compressional deformation of the upper lithosphere within the SPT and lithosphere-scale normal faulting at the margins. However, we emphasize that simple thermal expansion and contraction alone cannot explain the extensive tectonics within the SPT. The extensive tectonic modification and resulting large strains may indicate an earlier period of mobile-lithosphere tectonics[28,63].

Enceladus is much smaller than the Moon (radii of 252 and 1,738 km, respectively). Although the SPT is much smaller than the PKT in physical size (~300 km versus ~2,000 km), they are similar in angular size (Fig. 3). Thus, the geometric arguments for the formation of the quasi-rectangular PKT border structures due to the intersection of tectonic structures at 120° angles on a spherical surface may have relevance to the SPT as well. The different values of gravitational acceleration at the surfaces of the Moon and Enceladus would not directly affect their thermal evolution, but would have had an impact on the ensuing tectonic and volcanic processes.

Thus, we suggest that broadly similar geodynamic processes may have been at work in the PKT and the SPT. Both regions are characterized by strong thermal anomalies, enhanced volcanic activity, and low topography. The quasi-rectangular structures surrounding both provinces are consistent with the expected shapes of sets of tectonic structures intersecting at 120°-angle triple junctions. However, the specific evolutionary paths of the provinces were probably substantially different as a result of the differences in the sources of heat, temporal variations in heat flux, and rheologies of the lithospheres. Our current understanding of the formation and evolution of both structures is incomplete. Nevertheless, the two provinces highlight the important effect that regional thermal anomalies can have on the volcanic and tectonic evolution of quite different planetary bodies.

31. Lemoine, F. G. *et al.* GRGM900C: A degree 900 lunar gravity model from GRAIL primary and extended mission data. *Geophys. Res. Lett.* **41,** 3382–3389 (2014).
32. Reed, G. B. *Application of Kinematical Geodesy for Determining Short Wave Length Components of the Gravity Field by Satellite Gradiometry* (Tech. Rep. 201, Department of Geodetic Science, The Ohio State University, 1973).
33. Wieczorek, M. A. & Phillips, R. J. Potential anomalies on a sphere: applications to the thickness of the lunar crust. *J. Geophys. Res.* **103,** 1715–1724 (1998).
34. Kiefer, W. S. *et al.* The density and porosity of lunar rocks. *Geophys. Res. Lett.* **39,** L07201 (2012).
35. Parmentier, E. M., Zhong, S. & Zuber, M. T. Gravitational differentiation due to initial chemical stratification: origin of lunar asymmetry by the creep of dense KREEP? *Earth Planet. Sci. Lett.* **201,** 473–480 (2002).
36. Hess, P. C. & Parmentier, E. M. A model for the thermal and chemical evolution of the Moon's interior: implications for the onset of mare volcanism. *Earth Planet. Sci. Lett.* **134,** 501–514 (1995).
37. Elkins-Tanton, L. T., Burgess, S. & Yin, Q.-Z. The lunar magma ocean: reconciling the solidification process with lunar petrology and geochronology. *Earth Planet. Sci. Lett.* **304,** 326–336 (2011).
38. Elkins Tanton, L. T., Van Orman, J. A., Hager, B. H. & Grove, T. L. Re-examination of the lunar magma ocean cumulate overturn hypothesis: melting or mixing is required. *Earth Planet. Sci. Lett.* **196,** 239–249 (2002).
39. DeHon, R. A. Maximum thickness of materials in the western mare basins. *Proc. Lunar Planet. Sci. Conf.* **9,** 229–231 (1978).
40. Blakely, R. J. *Potential Theory in Gravity and Magnetic Applications* (Cambridge Univ. Press, 1995).
41. Hiesinger, H., Jaumann, R., Neukum, G. & Head, J. W. Ages of mare basalts on the lunar nearside. *J. Geophys. Res.* **105,** 29239–29275 (2000).

42. Hiesinger, H. *et al.* Ages and stratigraphy of mare basalts in Oceanus Procellarum, Mare Nubium, Mare Cognitum, and Mare Insularum. *J. Geophys. Res.* **108,** 5065 (2003).
43. Pritchard, M. E. & Stevenson, D. J. in *Origin of the Earth and Moon* (eds Canup, R. M. & Righter, K.) 179–196 (Univ. Arizona Press, 2000).
44. Toksöz, M. N., Dainty, A. M., Solomon, S. C. & Anderson, K. R. Structure of the Moon. *Rev. Geophys. Space Phys.* **12,** 539–567 (1974).
45. Presley, M. A. & Christensen, P. R. Thermal conductivity measurements of particulate materials: 4. Effect of bulk density for granular particles. *J. Geophys. Res.* **115,** E07003 (2010).
46. Besserer, J. *et al.* Theoretical and observational constraints on lunar mega-regolith thickness. *Lunar Planet. Sci.* **44,** abstr. 2463 (2013).
47. Turcotte, D. L. & Schubert, G. *Geodynamics* 2nd edn (Cambridge Univ. Press, 2001).
48. Buck, W. R. Modes of continental lithospheric extension. *J. Geophys. Res.* **96,** 20161–20178 (1991).
49. McGovern, P. J. *et al.* Impact-generated loading and lithospheric stress gradients at lunar impact basins: implications for maria emplacement scenarios. *Lunar Planet. Sci.* 44, abstr. 3055 (2013).
50. Wilson, L. & Head, J. W. Ascent and eruption of basaltic magma on the Earth and Moon. *J. Geophys. Res.* **86,** 2971–3001 (1981).
51. Lachenbruch, A. H. Mechanics of thermal contraction cracks and ice-wedge polygons in permafrost. *Spec. Pap. Geol. Soc. Am.* **70,** 1–66 (1962).
52. Spencer, J. R. *et al.* Enceladus heat flow from high spatial resolution thermal emission observations. *EPSC Abstr.* **8,** EPSC2013–2840-2011 (2013).
53. Spencer, J. R. *et al.* Cassini encounters Enceladus: background and the discovery of a south polar hot spot. *Science* **311,** 1401–1405 (2006).
54. Roberts, J. H. & Nimmo, F. Near-surface heating on Enceladus and the south polar thermal anomaly. *Geophys. Res. Lett.* **35,** L09201 (2008).
55. Tobie, G., Cadek, O. & Sotin, C. Solid tidal friction above a liquid water reservoir as the origin of the south pole hotspot on Enceladus. *Icarus* **196,** 642–652 (2008).
56. Thomas, P. C. *et al.* Shapes of the Saturnian icy satellites and their significance. *Icarus* **190,** 573–584 (2007).
57. Iess, L. *et al.* The gravity field and interior structure of Enceladus. *Science* **344,** 78–80 (2014).
58. Collins, G. C. & Goodman, J. C. Enceladus' south polar sea. *Icarus* **189,** 72–82 (2007).
59. Besserer, J., Nimmo, F., Roberts, J. H. & Pappalardo, R. T. Convection-driven compaction as a possible origin of Enceladus's long wavelength topography. *J. Geophys. Res. Planets* **118,** 908–915 (2013).
60. Nimmo, F., Spencer, J. R., Pappalardo, R. T. & Mullen, M. E. Shear heating as the origin of the plumes and heat flux on Enceladus. *Nature* **447,** 289–291 (2007).
61. Meyer, J. & Wisdom, J. Tidal heating in Enceladus. *Icarus* **188,** 535–539 (2007).
62. Lainey, V. *et al.* Strong tidal dissipation in Saturn and constraints on Enceladus' thermal state from astrometry. *Astrophys. J.* **752,** 14 (2012).
63. Barr, A. C. Mobile lid convection beneath Enceladus' south polar terrain. *J. Geophys. Res.* **113,** E07009 (2008).
64. Bland, M. T., Singer, K. N., McKinnon, W. B. & Schenk, P. M. Enceladus' extreme heat flux as revealed by its relaxed craters. *Geophys. Res. Lett.* **39,** L17204 (2012).
65. Giese, B. *et al.* Enceladus: an estimate of heat flux and lithospheric thickness from flexurally supported topography. *Geophys. Res. Lett.* **35,** L24204 (2008).
66. Crow-Willard, E. & Pappalardo, R. T. Global geological mapping of Enceladus. EPSC Abstr. **6,** EPSC–DPS2011-2635-2011 (2011).
67. Spencer, J. R. *et al.* in *Saturn from Cassini-Huygens* (eds Dougherty, M. K., Esposito, L. W. & Krimigis, S. M.) 683–724 (Springer, 2009).
68. Walker, C. C., Bassis, J. N. & Liemohn, M. W. On the application of simple rift basin models to the south polar region of Enceladus. *J. Geophys. Res.* **117,** E07003 (2012).
69. Yin, A. & Pappalardo, R. T. Left-slip faulting along the tiger stripe fractures: implications for the tectonic evolution of the south polar terrain, Enceladus. *Lunar Planet. Sci.* **44,** abstr. 1145 (2013).
70. Gioia, G., Chakraborty, P., Marshak, S. & Kieffer, S. Unified model of tectonics and heat transport in a frigid Enceladus. *Proc. Natl Acad. Sci. USA* **104,** 13578–13581 (2007).
71. Barr, A. C. & Preuss, L. J. On the origin of the south polar folds on Enceladus. *Icarus* **208,** 499–503 (2010).
72. Hurford, T. A. *et al.* Eruptions arising from tidally controlled periodic openings of rifts on Enceladus. *Nature* **447,** 292–294 (2007).

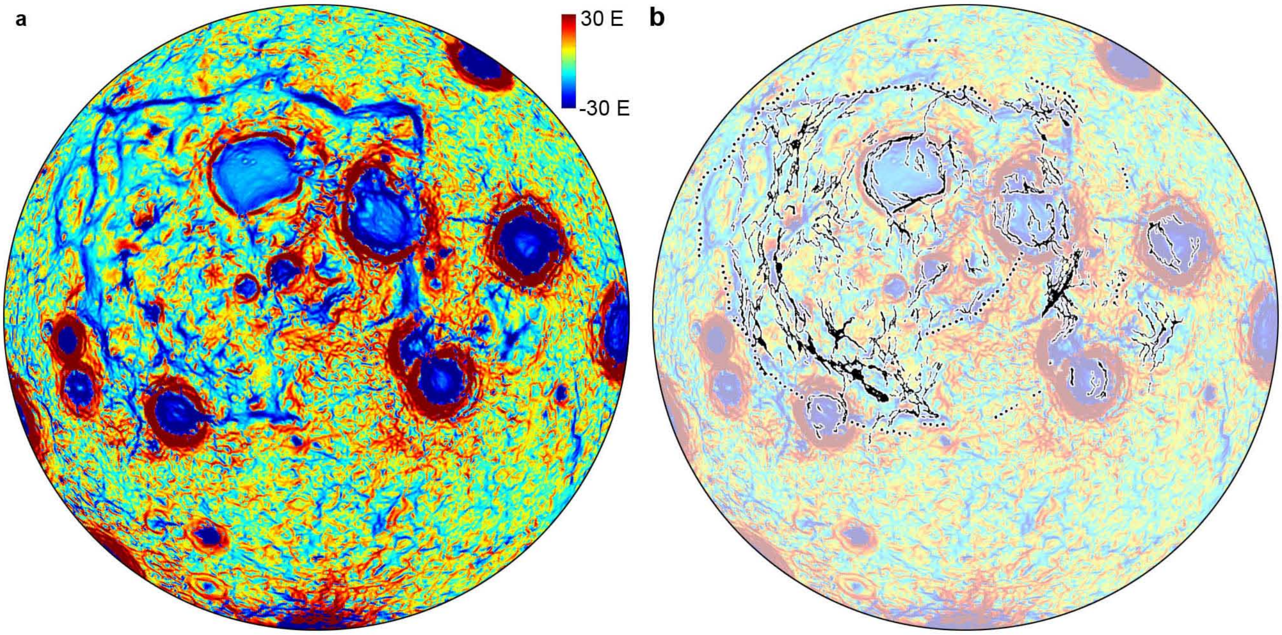

Extended Data Figure 1 | Comparison of the GRAIL gravity gradients with proposed Procellarum basin ring structures. **a**, Bouguer gravity gradients (in units of Eötvös; $1\ \mathrm{E} = 10^{-9}\ \mathrm{s}^{-2}$) on a Lambert azimuthal equal-area projection of the nearside of the Moon. **b**, Muted gravity gradients overlaid with mapped mare boundaries and scarps (dots) and wrinkle ridges (lines). Modified from figure 1 of ref. 5 with permission.

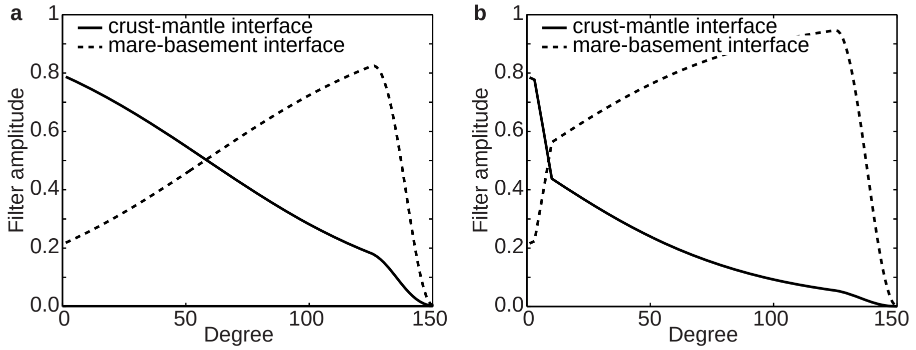

Extended Data Figure 2 | Amplitudes of filters applied during the crustal thickness modelling. **a**, **b**, Filters were applied during the calculation of the relief along the crust–mantle interface (solid lines) and the mare–basement interface (dashed lines) for cases in which the relief along the two interfaces was either isostatic before mare loading (**a**) or equal and opposite in amplitude (**b**). The filter in **b** imposes the isostatic condition from degrees 1 to 3 and a linear transition to the equal-amplitude filter from degrees 3 to 10. Both filters apply a cosine taper from degrees 125 to 150. The mare–basement filter is shown for illustration purposes only. In practice, the relief along the mare–basement interface was calculated from the residual Bouguer anomaly after the calculation of the crust–mantle interface relief (equivalent to using the filter shown with the original Bouguer gravity).

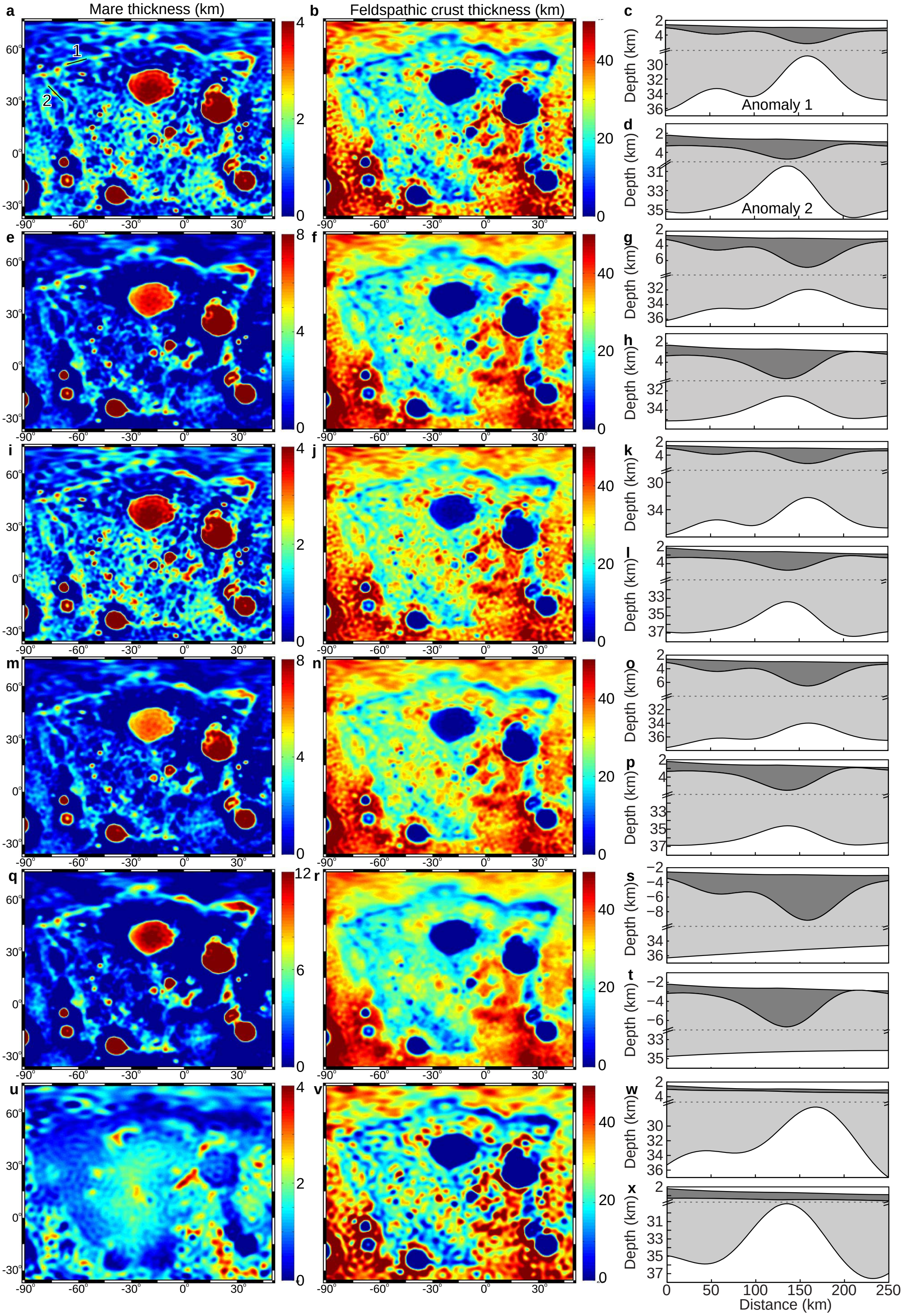

Extended Data Figure 3 | Predicted thicknesses of the crust and maria and average cross-sections across two of the border anomalies. Predicted thickness of the maria (left column) and underlying feldspathic crust (middle column), and cross-sections of the modelled structures of anomaly 1 (right column, top) and anomaly 2 (right column, bottom) showing the variations in the thicknesses of the mare (dark grey) and feldspathic crust (light grey). Models are for cases as follows: **a–d**, isostatic relief along the two interfaces before mare infilling with a mantle density of 3,220 kg m^{-3}; **e–h**, equal-amplitude relief along the two interfaces with a mantle density of 3,220 kg m^{-3}; **i–l**, isostatic relief along the two interfaces before mare infilling with a mantle density of 3,500 kg m^{-3}; **m–p**, equal-amplitude relief along the two interfaces with a mantle density of 3,500 kg m^{-3}; **q–t**, all gravity anomalies at degrees >10 ascribed to relief on the mare–basement interface; and **u-x**, all gravity anomalies at degrees >10 ascribed to relief on the crust-mantle interface.

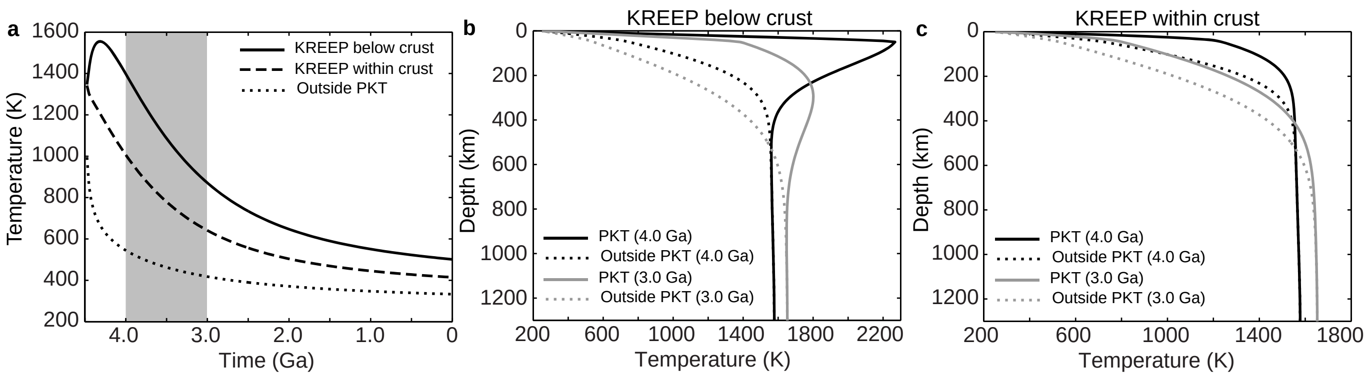

Extended Data Figure 4 | Temperature evolution within and outside the PKT. **a**, The temperatures as functions of time at a depth of 25 km are shown within the PKT for cases in which KREEP-rich material is either concentrated at the base of the crust (solid line) or is distributed throughout the crust (dashed line), as well as the temperature outside the PKT (dotted line). The period between 4.0 and 3.0 Gyr ago that is the focus of the stress modelling is indicated by the shaded box. **b**, **c**, The temperatures as functions of depth both inside and outside the PKT are shown for KREEP-rich material concentrated at the base of the crust (**b**) and for KREEP-rich material distributed throughout the crust (**c**).

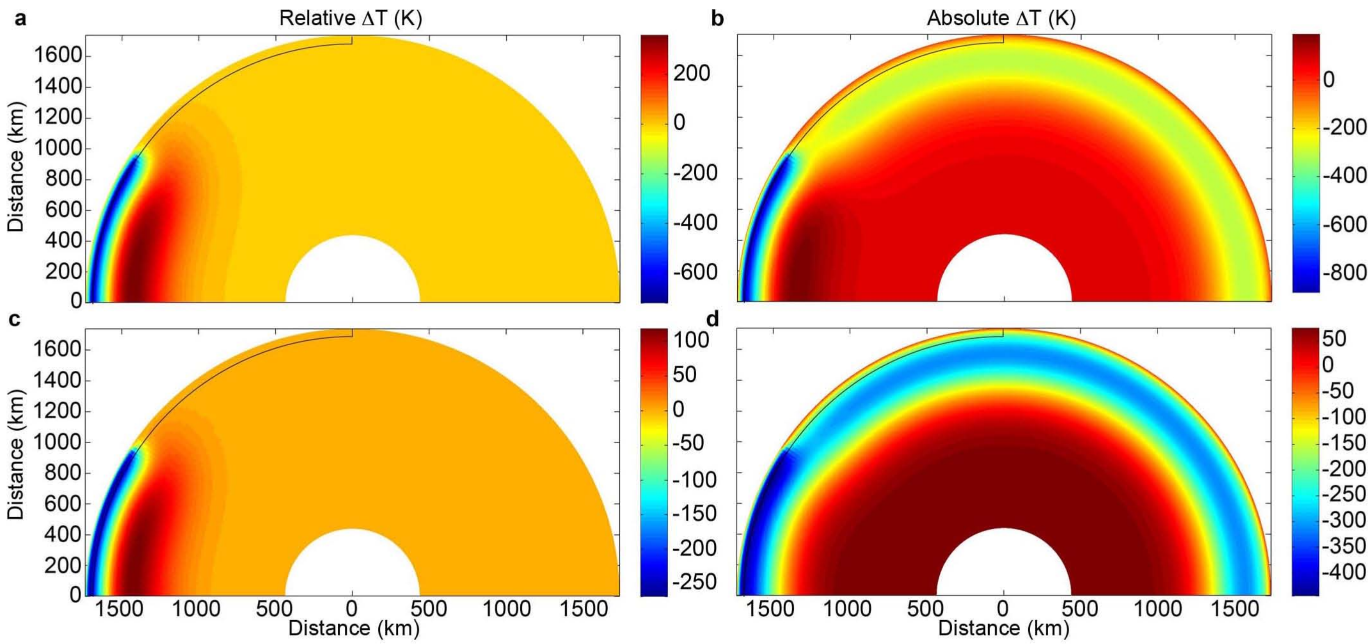

Extended Data Figure 5 | Predicted changes in temperature relative to areas outside the PKT and absolute temperature change between 4.0 and 3.0 Gyr ago. Results are shown for cases with KREEP concentrated at the base of the crust (**a**, **b**) and KREEP distributed throughout the crust (**c**, **d**). The PKT is centred on the pole at the left side of the panels. The region shown in Extended Data Figs 6 and 7 (encompassing 90° of arc extending radially outward from the centre of the PKT and downward to a depth of 50 km) is outlined in black.

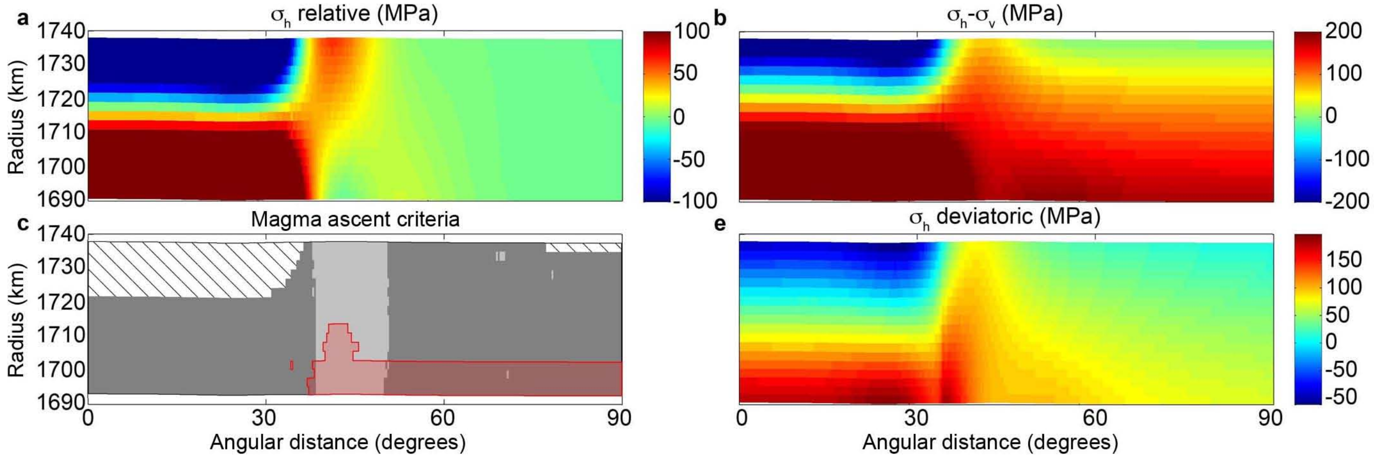

Extended Data Figure 6 | Predicted lithospheric stresses and magma ascent for the case of 10 km of KREEP at the base of the crust. Cross-sections show the following: **a**, the in-plane horizontal stresses (radial to the centre of the PKT, the far-field stress profile was subtracted to calculate the relative stress); **b**, the difference between the in-plane horizontal stress and the vertical stress; **c**, the magma ascent criteria; and **d**, the deviatoric stress. The magma ascent criteria in **c** reveal portions of the crust in which the horizontal stresses are tensile relative to the vertical stresses to permit the formation of vertical dykes (dark grey), where the vertical stress gradient is more favourable to magma ascent than the lithosphere far from the PKT (light grey), where magma will rise unassisted by other factors such as pressurized magma chambers (red), and where none of the criteria are satisfied (diagonal lines).

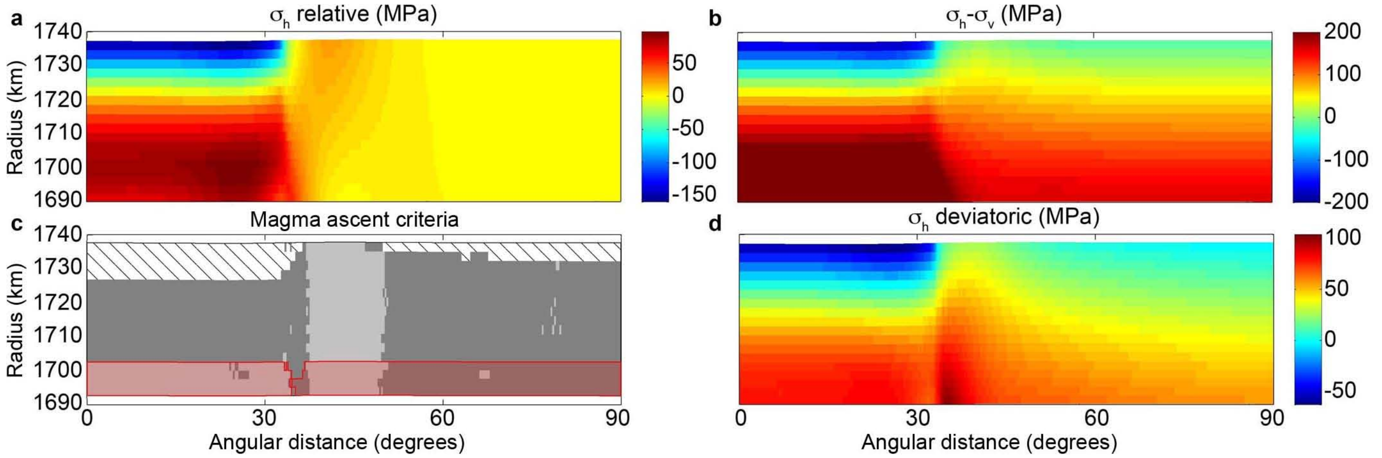

Extended Data Figure 7 | Predicted lithospheric stresses and magma ascent for the case of 10 km of KREEP basalt distributed uniformly through a 40-km-thick crust. All panels are as for Extended Data Fig. 6.

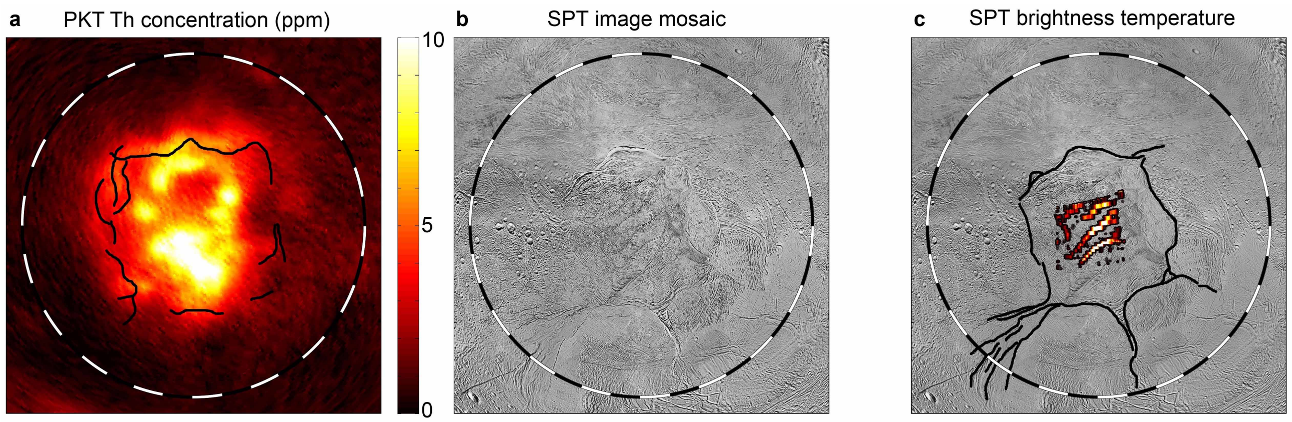

Extended Data Figure 8 | Additional comparisons of Procellarum KREEP terrane to the Enceladus south polar terrain (SPT). **a**, The PKT is characterized by high heat flow as a result of the enhanced abundances of radioactive elements[3] (represented by the concentration of thorium[4]). **b**, The border structures of the SPT as revealed by Cassini ISS images[24] also trace a quasi-rectangular pattern enclosing a region of elevated brightness temperatures and enhanced heat flow[26] (**c**) All maps are in a simple polar projection. In all panels, the circle corresponds to an angular diameter of 180° of surface arc, divided into 10° increments.

Extended Data Table 1 | Extension and strain across two border anomalies

Filter	ρ_M (kg/m^3)	Anomaly 1		Anomaly 2	
		extension	strain	extension	strain
isostatic	3220	15 km	0.11	13 km	0.08
equal amplitude	3220	12 km	0.09	10 km	0.07
isostatic	3500	11 km	0.09	10 km	0.06
equal amplitude	3500	11 km	0.08	9 km	0.06
mare-crust only	3220	10 km	0.07	8 km	0.05
crust-mantle only	3220	16 km	0.12	18 km	0.12